ABSTRACT

THERMAL ANALYSIS OF THERMAL SHIELD FOR PIP-II SSR1 CRYOMODULE

Victor Aguado, M.S
Department of Mechanical Engineering
Northern Illinois University, 2023
Nicholas A. Pohlman, Director

Fermilab's PIP-II project plans to enhance the onsite accelerator into the world's most intense neutrino beam, bringing Fermilab into the next generation of particle accelerators. The five different types of cryomodules are vital parts of the PIP-II project and each requires numerous engineering analyses to prove operation. For example, the thermal shield of the Single Spoke Resonator-1 (SSR1) cryomodule required a thermal analysis to ensure the design was operating as intended before fabrication commenced. The thermal shield is cooled by the supercritical helium inside of the extrusion and must remain between 45 and 80 Kelvin. The main purpose of the thermal shield is to intercept different high heat loads and thermal radiation and prevent them from reaching the more sensitive internal components. Finite Element Analysis (FEM) was used to determine temperature estimates of the thermal shield based on the location of a variety of heat sources. Results determined temperatures exceeding the design limit around the crucial component of the current leads. Due to superconducting properties, the areas around the current leads cannot surpass 68 Kelvin. Different solutions to the critical high-temperature areas will be proposed. These solutions range from changing the properties of the helium flow to designing an attachment for the thermal shield. Each

proposition works as a viable solution, however, each proposition also has its own set of advantages and disadvantages that are described for further design consideration.

NORTHERN ILLINOIS UNIVERSITY
DE KALB, ILLINOIS

DECEMBER 2023

THERMAL ANALYSIS OF THERMAL SHIELD FOR PIP-II SSR1 CRYOMODULE

BY

VICTOR AGUADO

A DISSERTATION SUBMITTED TO THE GRADUATE SCHOOL

IN PARTIAL FULFILLMENT OF THE REQUIREMENTS

FOR THE DEGREE

MASTER OF SCIENCE

DEPARTMENT OF MECHANICAL ENGINEERING

Dissertation Director:
Nicholas A. Pohlman

ACKNOWLEDGEMENTS

Most and foremost, I would like to thank the friends and family who helped me in getting to this point. It is thanks to your continued support and encouragement that I have made it as far as I have. I would also like to express my gratitude to all the different Fermilab employees who provided assistance and insight throughout the project. Josh Helsper deserves a special mention as an incredible mentor and confidante throughout the project. Lastly, I would like to thank my advisor, Nicholas Pohlman, for their guidance throughout and even before the start of the project.

TABLE OF CONTENTS

Page

LIST OF TABLES v

LIST OF FIGURES. vi

Chapter

1 INTRODUCTION 1

1.1 Fermilab 1

1.2 PIP-II 3

1.3 Thermal Shield 7

1.4 Previous Work 13

2 THEORY 15

2.1 Governing Equations 15

2.1.1 Conduction Heat Transfer 16

2.2 Ansys 23

2.3 Ansys Setup 25

2.3.1 Convection 26

2.3.2 Structures 32

3 METHODOLOGY 34

3.1 Evaluation Criteria 34

3.2 Structures 35

3.2.1 Extrusion 39

3.2.2 Shell pieces 40

Chapter Page

3.2.3 Covers and Ports 45

3.2.4 Thermal Straps 49

3.3 Heat Sources 52

3.4 Current Leads 56

4 RESULTS 59

4.1 Baseline Results 59

4.2 Helium Properties 62

4.2.1 Copper Plate Addition 66

5 CONCLUSION 75

5.1 Research Question 75

5.2 Summary and Reflection 75

5.3 Future Recommendations 77

LIST OF TABLES

Table Page

3.1 Spreadsheet containing data on the heat sources [31] 52

LIST OF FIGURES

Figure		Page
1.1	Diagram of the Fermilab accelerator complex [6]	2
1.2	Image of the niobium superconducting radiofrequency cavity [9]	4
1.3	PIP-II upgraded Linac [10]	5
1.4	Diagram of DUNE experiment [14]	6
1.5	Comparison of the different niobium cavities for each cryomodule [10], [16]	7
1.6	A look inside of a cryomodule [18]	8
1.7	Different images of the SSR1 prototype during testing at Fermilab	9
1.8	Diagram of the SSR1 internals [22]	10
1.9	SSR1 prototype during disassembly	12
2.1	3D cubic element used for Equation 2.1 showing the heat on each side of the cube [26]	17
2.2	Sketch of how an analysis of one of the upper shields may proceed	19
2.3	3D model showing the upper thermal shield part Figure 2.2 represents (in blue) and the r,ϕ, and z axes of the model	22
2.4	Plot showing how drastically the thermal conductivity of Aluminum 1100 can change at low temperatures [27]	26
2.5	Sketch of the extrusion cross section; red arrows represent conductive heat transfer from the upper and lower thermal shields; the blue arrows represent convective heat transfer between the inner diameter of the extrusion and the helium heat sink (purple).	27
2.6	Screenshot of data provided by NIST WebBook [28]	28

Figure Page

3.1 Cross section of the extrusion (F10151355) 36

3.2 Set-up of the node merge between the lower thermal shield and the welds (blue: contact edges; red: contact faces) 38

3.3 Triangular weld representation highlighted in green, the base of the weld is in contact with the extrusion via shell-to-solid contact, the vertical section is in contact with the lower thermal shield via solid body-to-solid body contacts 38

3.4 Labeled CAD model of the extrusion (F10147249) 39

3.5 Section of the upper thermal shield (F10191726) 40

3.6 Section of the lower thermal shield (F10147253) 41

3.7 NX sketch of upper thermal shield section (F10191726) 42

3.8 NX sketch of lower thermal shield section (F10147253). 43

3.9 All four lower shield connection brackets (F10147249) 44

3.10 Connection between the two lower thermal shield sections (a) lower shield connection in NX model (F10147249); (b) Lower shield connection in simulation 44

3.11 All three types of covers color coordinated (F10191721) 45

3.12 Edge to edge bonded contact 46

3.13 Edge to face bonded contact 46

3.14 Graphic showing the locations of the top port, side port, and end caps (F10191721) 48

3.15 Thermal shield bracket (F10191721) 48

3.16 Images showing an imprint on extrusion 50

3.17 Top port thermal strap comparison (a) thermal strap connecting one section of the top port to another (F10191721); (b) representation of top port thermal strap in the simulation 51

3.18 Support post heat load (a) Picture of support post CAD with two thermal straps (F10142933); (b) Support post heat load example in simulation. 54

Figure Page

3.19 Radiation heat load. 54

3.20 View port heat load (a) view port in SSR1 CAD model (F10142933); (b) view port heat load 55

3.21 Cyoport heat load (a) cryoport in SSR1 CAD model (F10142933); (b) cryoport heat load 56

3.22 Current lead heat load (a) current leads in SSR1 CAD model (F10142933); (b) current lead heat load 56

4.1 Baseline results of steady-state thermal simulation. 59

4.2 The increasing temperature of the helium within the extrusion where the horizontal sections correspond with transfer elbows 60

4.3 Results from Ansys showing the different temperatures on the extrusion and the name of the different sections 61

4.4 Thermal shield temperature results with a mass flow rate of 5.5 [g/s] 62

4.5 Graph visualizing the trend on the temperature of changing the mass flow rate (baseline conditions boxed with dashed lines); logarithmic trendline has a R^2 value of 98.16% 63

4.6 Thermal shield temperature results using a helium inlet temperature of 34 Kelvin 64

4.7 Graph visualizing the effects modifying the inlet temperature has on the thermal shield (baseline conditions boxed in dashed lines); linear trendline has a R^2 value of 100% 65

4.8 Baseline results back view, better view of high-temperature areas 66

4.9 High temperatures on the underside of the lower shield 67

4.10 Temperature difference between the extrusion and the end caps 68

4.11 Proposed copper plate idea and location within thermal shield NX model (F10191721) 68

4.12 Copper plate simulation (a) isometric view of the copper plate model; (b) side view of the copper plate model 69

4.13 Results of the first copper plate test assuming nearby connection points . . . 71

Figure Page

4.14 Thermal shield extrusion temperature probes 71

4.15 Lower thermal shield temperature probes 72

4.16 Comparison of different copper plate connection temperature results (a) plate connected to regions of the thermal shield around 60 Kelvin; (b) plate connected to regions of the thermal shield around 70 Kelvin 72

4.17 Plot showing the different thermal strap temperature tests 73

CHAPTER 1

INTRODUCTION

1.1 Fermilab

Fermi National Accelerator Laboratory (Fermilab) is a national laboratory funded by the United States Department of Energy. Located in Batavia, Illinois, Fermilab has been instrumental in particle physics research since its founding in 1967 [1]. Since 1972, Fermilab has had a particle accelerator operational, helping expand the understanding of particle physics. Research at Fermilab has been instrumental in the discovery of the top quark, the bottom quark, the tau neutrino, and the bottom omega baryon [2]. Research continues at Fermilab with experiments like the Muon g-2 experiment [3], the Holometer experiment [4], the Deep Underground Neutrino Experiment (DUNE) [5], etc.

A representation of the components within the accelerator complex can be seen in Figure 1.1. The four main accelerators that make up the complex are the Linac, the Booster, the Recycler, and the Main Injector. Currently, the Linac is a 500-foot linear accelerator that can bring proton beams up to 400 million-electronvolts (MeV). The proton beam begins right before the Linac and must cross the Linac to reach the rest of the accelerators. After the Linac, the proton beam enters the Booster. The Booster is a 1500-foot-circumference ring that accelerates the beam to an energy of 8 GeV. After the Booster, the proton beam then enters the Recycler. The Recycler is a 2-mile-circumference ring, and its purpose is to "slip stack" the proton beam. "Slip stacking" the proton beam combines batches of protons into a more intense beam, that can then enter the Main Injector. The Main Injector

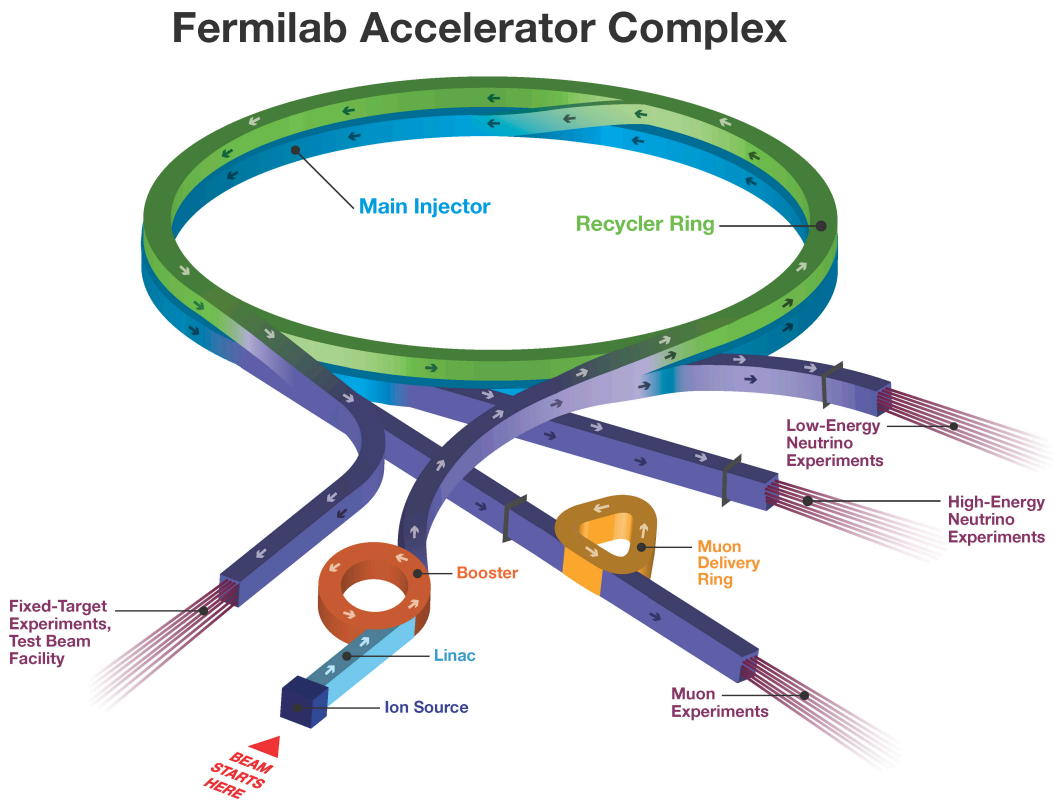

Figure 1.1: Diagram of the Fermilab accelerator complex [6]

is directly below the Recycler in the same tunnel and shares the same circumference. The purpose of the Main Injector is to bring the proton beam from 8 GeV to 120 GeV. Once the desired energy is achieved, the proton beam can then be delivered to the desired location of the particle experiment. This accelerator complex provides the world's most high-intensity neutrino beams.

Out of all four main accelerators that make up the Fermilab complex, the Linac is currently the section in most need of an upgrade. The Recycler and the Main Injector replaced the Main Ring, Fermilab's first primary accelerator, in 1999 [7]. Construction on the Booster

ended in 1970, and the Booster achieved its design energy in 1971. Meanwhile, the Linac finished construction in 1969 and is the oldest, still running, section of the accelerator. The Linac had a small upgrade in 1993 doubling the design energy from 200 MeV to 400 MeV. However, the 1993 upgrade does not compare to the intensive work done when replacing the original Main Ring. The Proton Improvement Plan II (PIP-II) plans to replace the Linac and bring Fermilab into the next generation of particle accelerators.

1.2 PIP-II

The PIP-II project plans to enhance Fermilab's accelerator complex into the world's most intense neutrino beam. The design energy of the new PIP-II Linac is set at 800 MeV, double the design energy of the current Linac [8]. The niobium-tin superconducting radiofrequency (SRF) cavities are an important component of how such high energies are reached. Niobium is an element that becomes superconducting at ultra-low temperatures. At less than 4 degrees Kelvin, the niobium cavities become superconducting, meaning they have zero electrical resistance. A cavity with zero electrical resistance is desired since then there is no energy lost due to heat. Limiting the amount of energy lost helps ensure more energy goes towards powering the beam. Figure 1.2 shows an image of one of these niobium cavities. There are 5 different types of niobium cavities used in total. The number of cells and distance between the cells can change depending on the cryomodule the cavity is in and the estimated energy/speed of the proton beam at that location. The kinetic energy of the beam is measured in electron-volts (eV), as the kinetic energy of the beam increases so does its speed. As the speed of the beam increases the distance between the cavity cells also increases since the beam covers more distance.

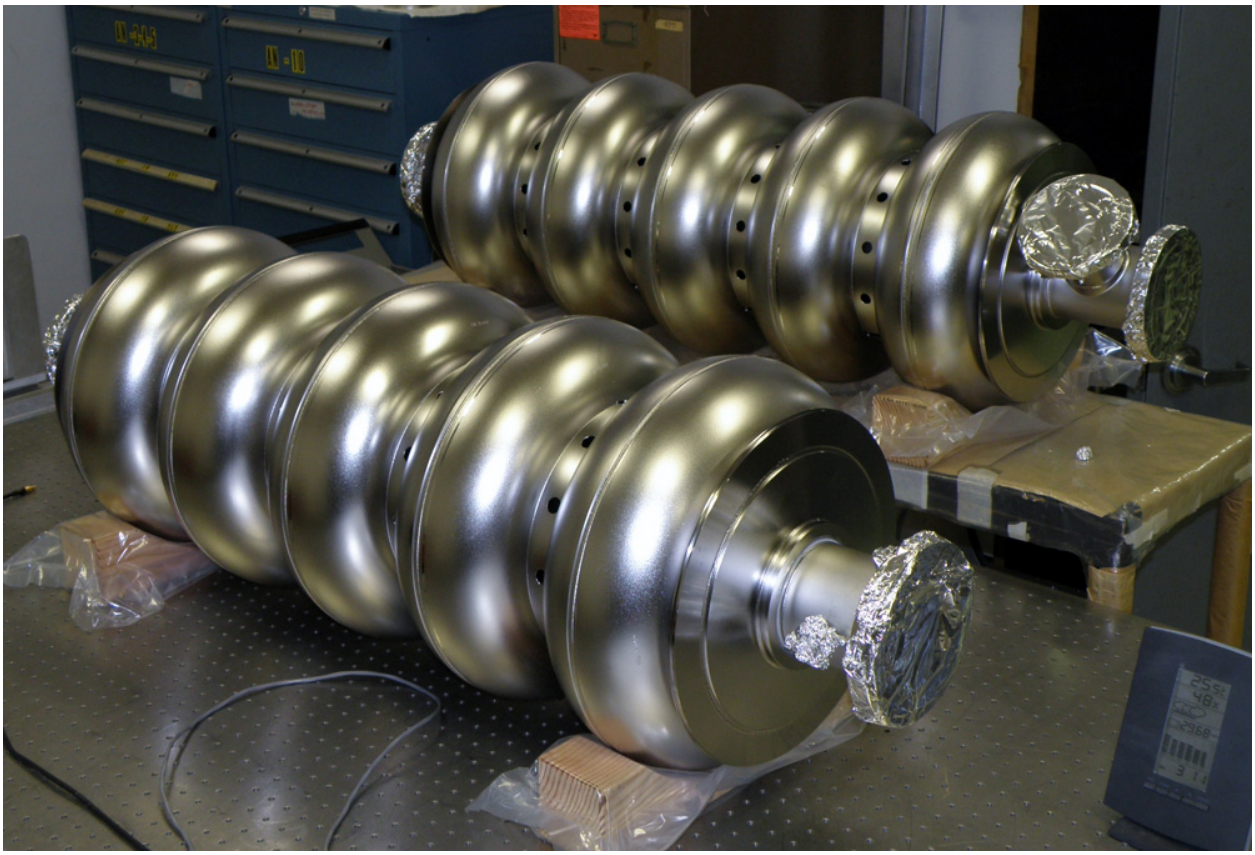

Figure 1.2: Image of the niobium superconducting radiofrequency cavity [9]

Construction of the PIP-II complex began in March 2019 and is scheduled to be completed in 2028. Once completed the new PIP-II Linac will span 215 meters and produce a proton beam with an instantaneous beam power of over 1 megawatt traveling up to 92% the speed of light. The 215-meter span of the PIP-II Linac will consist of 5 different cryomodule types. The sequence of cryomodules along the beamline is indicated through the image seen in Figure 1.3.

The PIP-II project is not just a Fermilab centric project, but also a collaboration between many international partners [11]. The Cryoplant cooling the helium into its liquid phase will be designed and constructed by the Department of Atomic Energy in India, meanwhile, the Cryogenic Distribution System (CDS) that transports the liquid helium will be designed by

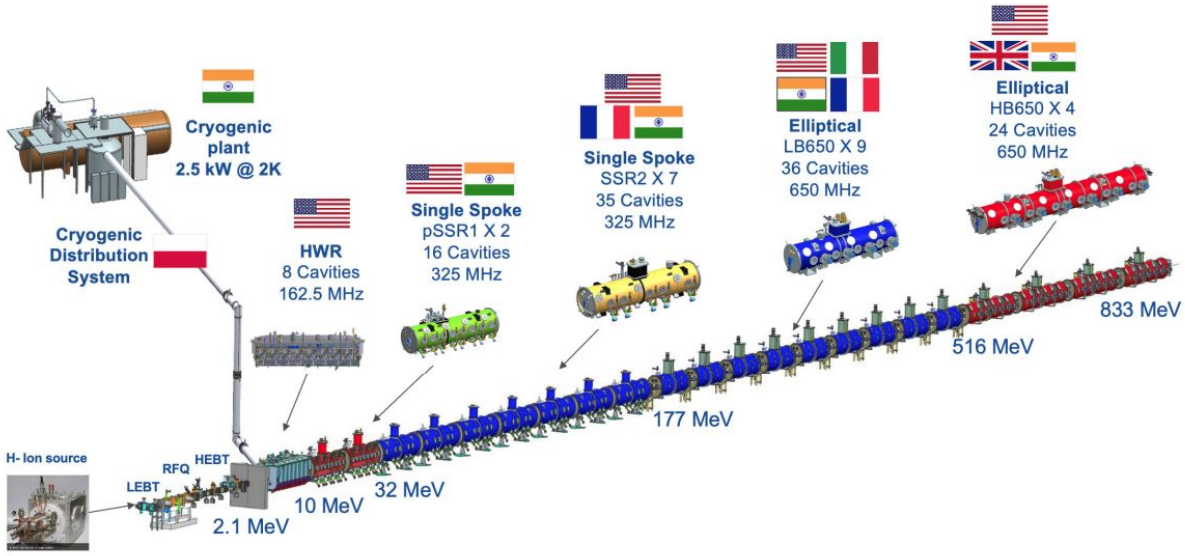

Figure 1.3: PIP-II upgraded Linac [10]

the Wroclaw University of Science and Technology in Poland. The Half-Wave Resonator (HWR) cryomodule will be designed and constructed by Argonne National Laboratory here in the US. The Single Spoke Resonators type 1 (SSR1) cryomodules will be constructed at Fermilab with help from Indian organizations. The Single Spoke Resonators type 2 (SSR2) cryomodule will be constructed as a collaboration between Fermilab and organizations from France and India. The Low Beta 650 MHz (LB650) cryomodule will be developed as a collaboration between Fermilab and organizations from France, India, and Italy. Lastly, the High Beta 650 MHz (HB650) cryomodule will be constructed as a collaboration between Fermilab and organizations from India and the United Kingdom [10].

The PIP-II project along with future upgrades aims to triple Fermilab's current beam power. The upgrades would also increase the amount of protons generated by the accelerator, allowing for an increase in flexibility and the amount of research projects that can be conducted. The big project that the new PIP-II Linac will be a vital component of is the Deep Underground Neutrino Experiment (DUNE) [12]. This experiment plans to unlock the mysteries of the neutrino. Fermilab will produce the neutrino beam onsite and send this

beam 1300 kilometers away to the Sanford Underground Research Facility in South Dakota [13]. A diagram showing this experiment can be seen in Figure 1.4. The data gathered from the DUNE near detector at Fermilab and the DUNE far detector underneath the Sanford Underground Research Facility will be instrumental to the research on the origin of matter, proton decay, and the formation of black holes. Without the PIP-II Linac upgrades, the DUNE experiment would not be possible.

The DUNE experiment will not be the only experiment the upgraded PIP-II Linac will assist. The upgrade Linac can deliver more than the required amount of protons needed for the DUNE experiment [15]. The excess protons can then be used for other research projects at Fermilab. For example, protons at an energy of 800 MeV could be delivered to the upcoming Mu2e experiment, or the protons can be accelerated further and used in neutrino and muon research. In conclusion, the PIP-II project will enable Fermilab to investigate a broader range of phenomena and usher in the next generation of particle accelerator technology.

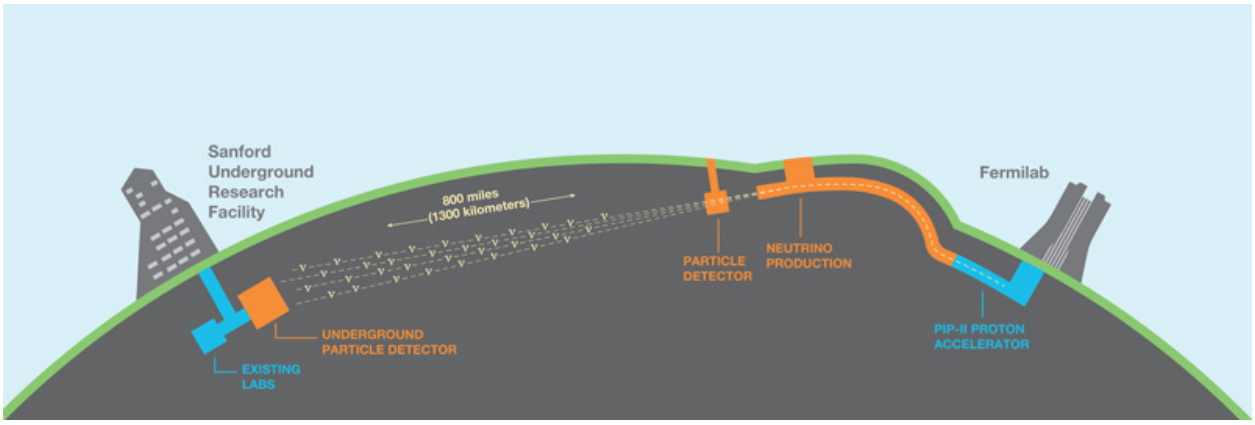

Figure 1.4: Diagram of DUNE experiment [14]

1.3 Thermal Shield

The objective and benefits of PIP-II have been discussed. However, the actual upgrades PIP-II promises have only been slightly explored. The new cryomodules that are planned to be constructed for PIP-II are crucial components of the upgrade. In total, there will be 23 cryomodules of 5 different types [9]. There is one HWR cryomodule, two SSR1 cryomodules, seven SSR2 cryomodules, nine Lb650 cryomodules, and four Hb650 cryomodules. The purpose of the cryomodules is to house the niobium cavities and ensure they operate uninterruptedly. A comparison between the five different niobium cavities can be seen in Figure 1.5.

In order to ensure the niobium cavities remain operational, a variety of different instruments must also be contained in the cryomodules. These instruments range from magnets to pumps, to wires, to pipes, etc. The niobium cavities and the instruments inside all require

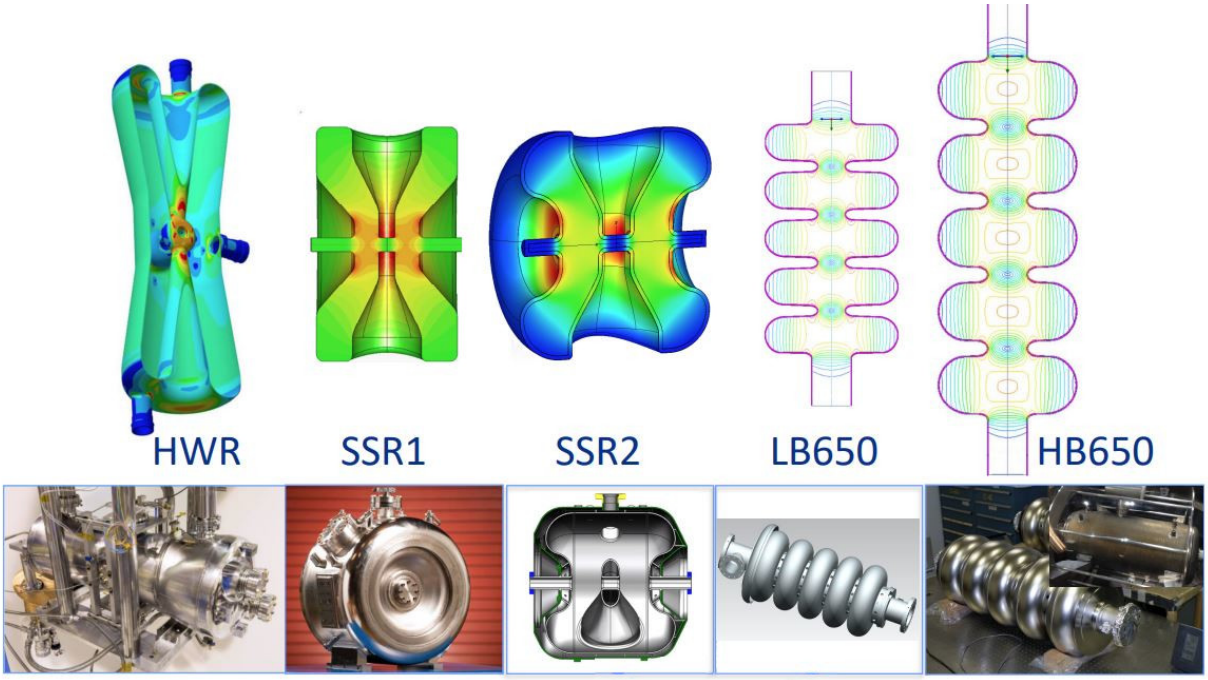

Figure 1.5: Comparison of the different niobium cavities for each cryomodule [10], [16]

certain conditions to remain operational [17]. For example, the niobium cavities must remain under around 9 Kelvin to remain superconducting. The cryomodule must also sustain a vacuum inside. The cryomodules must be specially constructed to meet all of these criteria. A few of the criteria all five cryomodules must meet are providing support, being precise in their alignment of the cavities, minimizing vibration, providing magnetic shielding, keeping the internals from exceeding allowable pressures, providing insulation, and intercepting significant heat loads [17]. Designing these cryomodules requires expertise in mechanical, thermal, and electrical engineering, Figure 1.6 gives a look into the complexity that goes into one of these cryomodules.

This paper will specifically focus on elements within the SSR1 cryomodule. The SSR1 cryomodule is the second type of cryomodule in the beamline sequentially. There are two

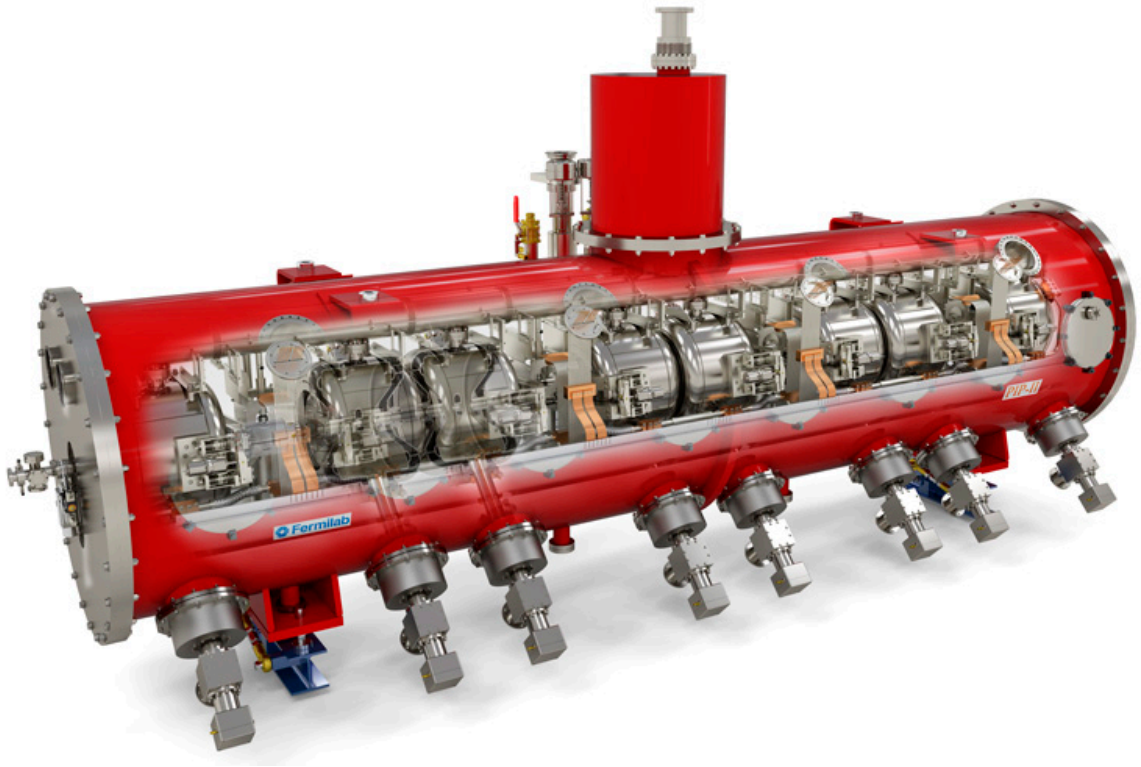

Figure 1.6: A look inside of a cryomodule [18]

SSR1 cryomodules in the beamline, both operating at 325 MHz, double that of the HWR. The SSR1 cryomodules accept the H-minus beam from the HWR at 10 MeV and accelerate the beam to around 32 MeV. The SSR1 cryomodule is one of two types of cryomodules that house single-spoke resonators (SSR), the other being the SSR2 cryomodule. The HWR cryomodule uses a half-wave resonator and the Lb650 and Hb650 cryomodules both use elliptical cavities. Both the SSR1 and SSR2 house single-spoke resonators inside the cryomodules. The reason they are two different cryomodules is that the cavities need to differ to account for the increasing velocity of the beam. A prototype of the SSR1 cryomodule has been built and tested at Fermilab. Figure 1.7 shows some images from the tests.

The SSR1 cryomodule is also the first cryomodule in the beamline to use the new cylindrical cryomodule design. The HWR cryomodule is a top-loaded box cryomodule, meanwhile,

(a) [19]

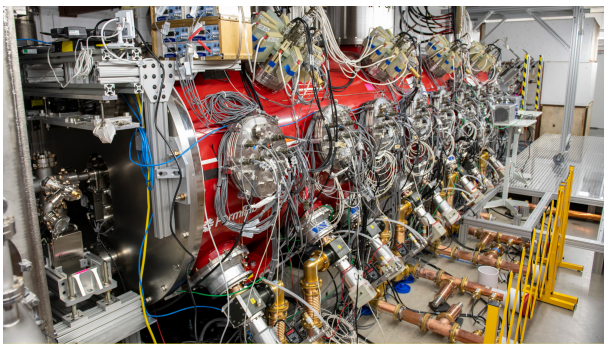

(b) [20]

(c) [21]

(d) [21]

Figure 1.7: Different images of the SSR1 prototype during testing at Fermilab

all the other cryomodules in the beamline use the new cylindrical design. This cylindrical design purposely has all external connections to the cryogenics, RF, and instrumentation systems made at removable junctions.

The SSR1 cryomodule was the first cryomodule designed within this framework. Figure 1.8 shows a labeled diagram of some of the components inside the SSR1 cryomodule. All other cylindrical cryomodules in the beamline were based on the SSR1's design [10], [23]. Since all cylindrical cryomodules are based on the SSR1's design, they all share design philosophy on the structure and components. For example, the support post, vacuum vessel,

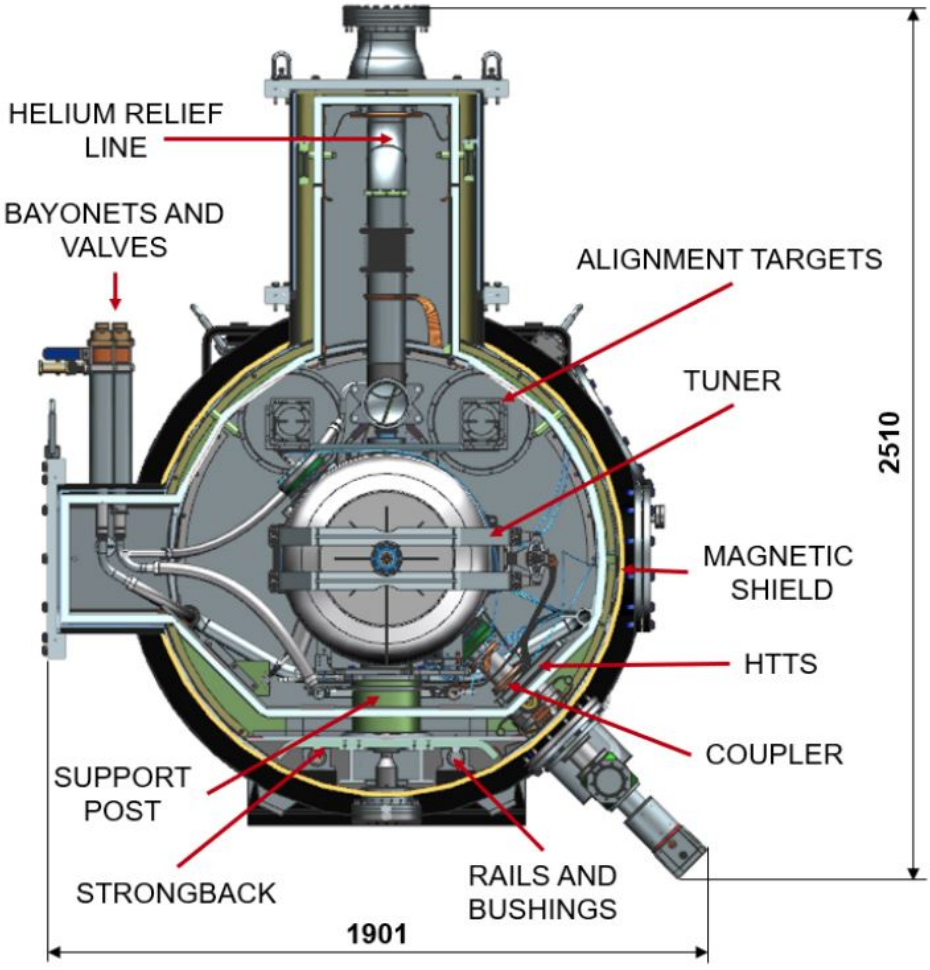

Figure 1.8: Diagram of the SSR1 internals [22]

cryogenic pumping, and thermal shields' of all the cylindrical cryomodules resemble each other. Understanding the cryomodules becomes simpler due to this similarity since grasping the layout of a single cryomodule allows one to understand the layout of all the cryomodules.

The cylindrical cryomodules have various methods of cooling and insulating the internal components [23], [24]. The different temperature cooling lines inside of the cryomodules are one way the internals are kept at their required temperature ranges. There is a 35 Kelvin - 50 Kelvin line, a 5 Kelvin line, and a 2 Kelvin line all of which are cooled using extremely cold helium. The helium is fed to these lines from the external Cryogenic Distribution System (CDS), and the lines are used to keep the sensitive internal components cold. Thermal insulation is also used inside the cryomodules to keep the internals cool. In the layer after the vacuum vessel, there are two 15-layer blankets of multi-layer insulation (MLI). MLI is typically made from double-aluminized mylar with fabric, nylon, or spun-bonded material spacers. The purpose of the MLI is to reduce the thermal radiation from the room-temperature vacuum vessel. The thermal shield, made from aluminum 1100, is the next layer after the MLI and also reduces the thermal radiation from higher-temperature components.

This paper will specifically focus on the thermal shield of the SSR1 cryomodule. The thermal shields need to differ between the cryomodules to account for the differences of the cryomodules. These differences include the amount of cavities, the size of the cryomodules, etc. When the accelerator is running, the thermal shield's temperature must range from 45 Kelvin to 80 Kelvin. The thermal shield is cooled via multiple welds with the 35 Kelvin - 50 Kelvin line. The purpose of all the thermal shields is to intercept different heat loads and thermal radiation. By intercepting these high temperatures, the thermal shield is able to reduce the heat loads the internal components receive. Intercepting these larger heat loads with the thermal shield is beneficial to the overall system. Keeping the thermal shield's 35 Kelvin - 50 Kelvin cooling line at the appropriate temperature range is easier and more

affordable than maintaining the temperature ranges of the colder cooling lines. Sections of a thermal shield can be seen in Figure 1.9. This thermal shield is of the SSR1 prototype and the image was taken at Fermilab during the disassembly of the cryomodule.

The goal of this paper is to analyze the thermal performance of the SSR1 thermal shield while the accelerator is operating. Analysis has already been done on other thermal shield designs, however, results are required for this specific SSR1 thermal shield design. The analysis must verify if the thermal shield design and parameters meet the necessary evaluation criteria. If the analysis finds that the evaluation criteria are not met, suggestions and remedies are to be suggested.

Figure 1.9: SSR1 prototype during disassembly

1.4 Previous Work

This paper is not the first analysis of a Fermilab thermal shield or cryomodule. Specifically, the master's theses of two Northern Illinois University (NIU) graduate alumni were instrumental sources of knowledge. Both of these theses provide valuable information and guidance for the analysis and documentation of this paper.

Gerald Smith's 2020 master's thesis on the thermal and structural analysis of the Hb650 thermal shield provided an introduction and understanding of similar analyses of the past [25]. Gerald's thesis focused on the welds connecting the upper and lower thermal shield of the Hb650 cryomodule to the extrusion. The thesis contained a steady-state thermal analysis, a transient thermal analysis, a static structural analysis, and a structural buckling analysis to analyze and optimize the welds on the thermal shield. The optimizations and modifications recommended were adopted into the design of the Hb650 cryomodule, and are also planned additions to the designs of other cryomodule thermal shields. For example, one of the reasons why this thermal analysis of the SSR1 thermal shield was warranted was to test the design changes from Gerald's work. Both an instrumental basic understanding of the Fermilab cryomodules and the thermal shields were acquired from Gerald's thesis. This thesis mainly focuses on a steady-state thermal analysis of the SSR1 thermal shield, a similar analysis was conducted and detailed in Gerald's thesis. The information about the steady-state thermal analysis of the Hb650 cryomodule was an irreplaceable asset for the SSR1 thermal shield analysis and provided a source of comparison and useful knowledge in the setup of the analysis.

Josh Helsper's 2020 master's thesis on the transportation analysis of the Hb650 cryomodule was also a very beneficial resource for this paper. Josh's thesis focused on an Ansys analysis of the transportation of the Hb650 cryomodule. Since the Hb650 cryomodules will

need to be transported on the road for construction and assembly, a transport analysis ensures the cryomodules remain intact. During the analysis, the cryomodule is split into sub-assemblies which can be analyzed individually or all together. Josh's analysis focuses on the stresses and vibrations the Hb650 cryomodule will experience when in transport, and optimize the positioning of the cryomodules while in transport. While Josh's analysis did not deal with any sort of thermal analysis, it does provide a plethora of useful knowledge about the workings of the Fermilab cryomodules and the setup of similar Ansys simulations.

CHAPTER 2

THEORY

2.1 Governing Equations

Estimating the temperature, a product will experience and ensuring the product remains functional as intended is a vital process of any design review. Since physical testing would cost too much money and time, theory and math must be relied on for estimates. For an object as complex as the SSR1 thermal shield, the methods of analysis can become very elaborate and time-consuming.

Before starting an analysis, the workings of the system in question need to be understood. In this case, the sources of temperature change within the thermal shield must be understood. The thermal shield is constantly in a balance between heat loads, warming up the thermal shield, and supercritical helium, cooling the thermal shield, in order to remain at a desired temperature range.

The helium that circulates the thermal shield starts at its coldest temperature and is delivered from the cryoplant facility. As the helium traverses the thermal shield, cumulative energy is transferred from the thermal shield into the helium. This process is the main cooling method of the thermal shield, and the temperature of the thermal shield can be regulated. The helium inside of the extrusion is in supercritical liquid form, therefore, the heat transfer for the helium is represented as convection.

The convection of the helium cools the thermal shield from various sources of heat including both thermal radiation and conduction. The thermal radiation comes from the large

temperature difference between the cold thermal shield and the outside of the cryomodule. Meanwhile, the heat coming from conduction arises from hotter components inside the cryomodule being connected to the thermal shield. Conduction also leads the heat of the thermal shield to the extrusion via the welds connecting both components.

The flow of the supercritical helium cools the extrusion via convection. The welds connecting the extrusion to the upper and lower thermal shields then provide a path for the heat of the thermal shield to reach the extrusion. The heat transfer between the extrusion and thermal shield is dependent on the conduction of the welds connecting both sections. Both the convection of the helium and the conduction between the different materials of the thermal shield are temperature-dependent. The temperature of the helium continuously increases as it traverses the thermal shield meaning both the convection and conduction are also dependent on the location of the helium within the thermal shield. The convection coefficient differs even more, unlike the thermal conductivity that can be found within a data table, the convection coefficient must be derived. The process of deriving the convection coefficient will be discussed in more detail in Section 2.3.1, all that needs to be known right now is that the derivation adds new parameters.

2.1.1 Conduction Heat Transfer

In order to begin the thermal analysis of the thermal shield, an equation involving heat in all 3 dimensions is required. Performing an energy balance of the thermal shield is the first step to arriving at the necessary equation. The energy balance needed must account for all the heat entering and leaving the system. For example, an energy balance of a section of the extrusion would treat the heat coming from the welds as heat entering the system (Q_{in}). Meanwhile, the heat transfer from the convection of the helium would be treated as heat

leaving the system (Q_{out}). Since the system is in equilibrium, Q_{in} and Q_{out} must equal one another determining the exit temperatures of the helium throughout the system. (Q_{in}) and (Q_{out}) are both capital Qs since they represent the heat for their overall system and are the integration of all the local heat (q) values of the system.

$$q_x + q_y + q_z + q_{gen} = q_{x+dx} + q_{y+dy} + q_{z+dz} + \frac{\partial E}{\partial t} \tag{2.1}$$

Equation 2.1 shows the results of an energy balance conducted on a simple cubic 3D element that can be seen in Figure 2.1 [26]. A 3D cubic element was used due to its simplicity, the information found using the cubic element can also be applied to the thermal shield analysis. The cubic nature of the element used for the energy balance requires the heat from each face of the element to be considered. For this reason, there are two heat terms in the

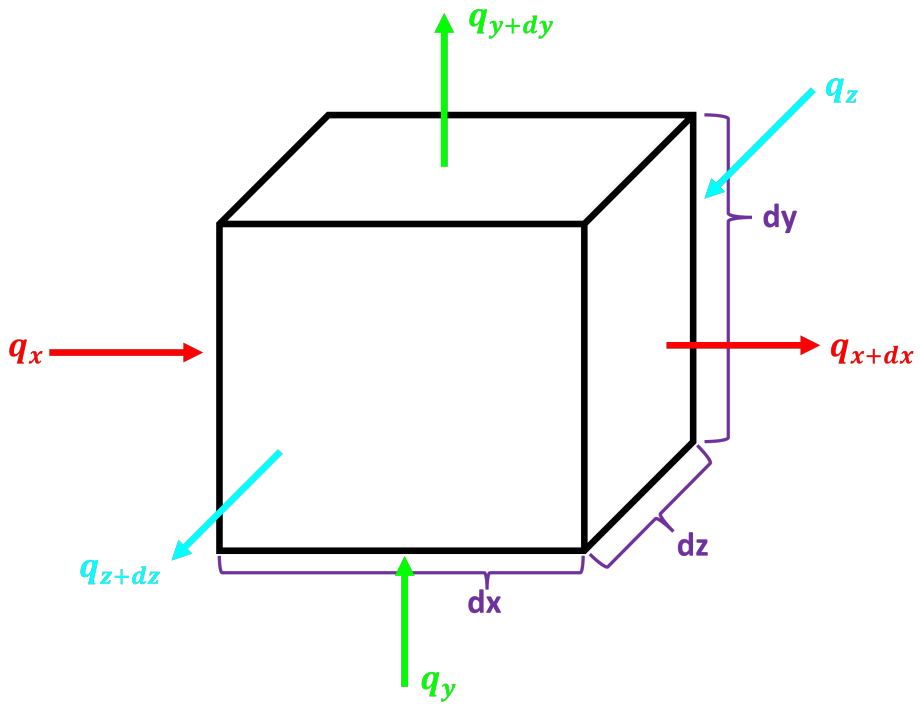

Figure 2.1: 3D cubic element used for Equation 2.1 showing the heat on each side of the cube [26]

x-direction (q_x and q_{x+dx}), one for the face of the cube on the x-axis and the other for the face facing the x-axis but also a distance of dx away. The heat in the y and z directions also gets the same treatment resulting in $q_y, q_{y+dy}, q_z, and\ q_{z+dz}$. Equation 2.1 must also consider the heat generation of the element (q_{gen}) and the change in internal energy of the element over time ($\frac{\partial E}{\partial t}$).

$$q_x = -k\ d_y\ d_z\ \frac{\partial T}{\partial x} \tag{2.2}$$

$$q_{x+dx} = -[k\frac{\partial T}{\partial x} + \frac{\partial}{\partial x}(k\frac{\partial T}{\partial x})\ d_x]d_y\ d_z \tag{2.3}$$

$$q_{gen} = \dot{q}\ d_x\ d_y\ d_z \tag{2.4}$$

Equations 2.2 - 2.4 show how the parameters for Equation 2.1 are found. Equations 2.2 and 2.3 show the formulas for both the heat parameters in the x-direction, the remaining heat parameters in the y and z directions follow the same equation layout as Equations 2.2 and 2.3. The directional heat parameters contain the thermal conductivity (k), the area of the heat flow represented by the differentials of the two other directions (dy and dz in the case of the x-direction), and the change in temperature in that direction ($\frac{\partial T}{\partial x}$). Equation 2.4 shows the formula for the heat generations (q_{gen}) parameter in Equation 2.1 which contains the heat flux ($\dot{q}$) of the system. The thermal analysis of the thermal shield will only consider the temperature of the thermal shield at its highest. For this reason, the internal energy change seen in Equation 2.1 goes to zero.

$$\frac{\partial}{\partial x}(k\frac{\partial T}{\partial x}) + \frac{\partial}{\partial y}(k\frac{\partial T}{\partial y}) + \frac{\partial}{\partial z}(k\frac{\partial T}{\partial z}) + \dot{q} = 0 \tag{2.5}$$

Combining Equations 2.1 - 2.4 results in Equation 2.5. The heat transfer in all three dimensions and heat generation are accounted for in the left side of Equation 2.5. Mean-

while, since the analysis is steady-state the right side of Equation 2.5 is set at zero. Using Equation 2.5, an accurate 3D thermal analysis can be started for the thermal shield.

Each part on the thermal shield would need to be analyzed using Equation 2.5. The difficulty and complexity of the analysis of just one part is already high. A complete thermal shield analysis would require each part of the thermal shield to be analyzed and the connection and interaction between each part also to be evaluated.

Figure 2.2 shows a proposition of how an analysis of one of the parts of the thermal shield may proceed. The specific section detailed in Figure 2.2 is the upper thermal shield closest to the inlet location of the helium. The upper shield section was split in half due to the large differences in temperature between the helium on each side. The helium on the

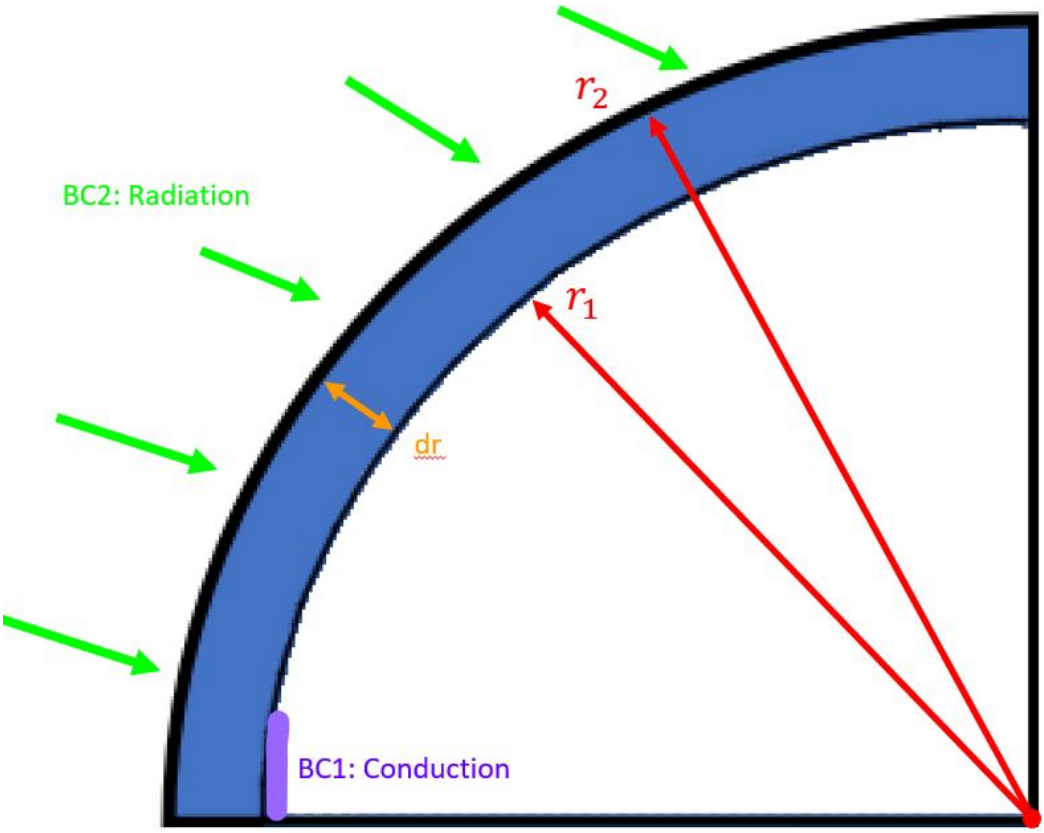

Figure 2.2: Sketch of how an analysis of one of the upper shields may proceed

half that was kept is the closest to the inlet temperature. Meanwhile, the temperature of the helium on the other half is unknown. The helium on the other half will have already traveled through about half of the thermal shield, gaining much heat along the way. The idea behind this setup would be to analyze the sections along the path of the helium.

Figure 2.2 also shows the different boundary conditions that would be used in the analysis of a section of the upper thermal shield. The cooling from the helium inside of the extrusion is represented by the purple conduction boundary condition. The convection of the helium inside of that section of the extrusion would have to first be analyzed before the conduction boundary condition could be implemented. Meanwhile, the radiation boundary condition in green represents the heat radiation from outside of the cryomodule that the thermal shield was built to block. Due to the circular geometry of the upper shield, a form of Equation 2.5 in cylindrical coordinates is more useful.

$$\frac{1}{r}\frac{\partial}{\partial r}(k\ r\frac{\partial T}{\partial r}) + \frac{1}{r^2}\frac{\partial T}{\partial \phi}(k\frac{\partial T}{\partial \phi}) + \frac{\partial}{\partial z}(k\frac{\partial T}{\partial z}) + q_{gen} = 0 \tag{2.6}$$

Equation 2.6 shows the cylindrical coordinate version of Equation 2.5. Cylindrical coordinates are typically used for circular geometries and deal in radius (r), phi (ϕ), and z instead of the x,y, and z seen in Equation 2.5. r specifies the radial distance of the desired location, ϕ specifies the angle of the desired location, and z specifies the height/depth of the desired location. Using r,ϕ, and z allows for the locations on the circular upper shield sections to be more easily defined and makes the analysis for these sections more straightforward.

The analysis of the upper shield section represented in Figure 2.2 may require many different assumptions. Assumptions and estimations will have to be made when analyzing the connections and interactions between the different parts of the thermal shield. If the thermal shield is split into smaller sections, assuming the temperature of the helium inside of those sections remains constant would lessen the burden of the derivation. A constant

helium temperature would also result in constant values for the helium's thermal conductivity and convection coefficient. However, assuming constant values also introduce error in the estimation.

The decision on how to divide the thermal shield for analysis is challenging. An analysis of each part of the thermal shield is already required, however, as shown in Figure 2.2, dividing the parts into smaller sections makes the derivations simpler but also increases the number of derivations. Figure 2.2 only shows the r and ϕ axes of the upper shield section, the z axis has not yet been considered. The division seen in Figure 2.2 removed half of the upper shield in the phi axis. This removal would make the analysis of the remaining geometry seen in Figure 2.2 more straightforward, however, the division also increases the number of derivations since the other half also needs to be analyzed and the interaction between the two halves also needs to be analyzed.

The r and ϕ axes of the upper thermal shield have been discussed, however, the z-axis, seen in Figure 2.3, still needs to be considered. The z-axis in this scenario would account for the depth of the part of the upper shield. The easy route for this analysis would be to assume a constant thermal conductivity and use the depth of the entire upper shield part for the analysis, However, using such a large section would decrease the accuracy of the analysis. The temperature and by effect the thermal conductivity of each location on the thermal shield are different. The larger the sections begin analyzed, the less accurate the analysis becomes if the properties for those sections are assumed constant. "Slicing" the parts of the thermal shield along the z-axis would lessen the effect on the accuracy of the analysis since an increase in the number of sections also increases the amount of location-specific properties that are included in the analysis. However, increasing the number of sections also increases the amount of analyses required and the amount of interactions between sections that need to be analyzed.

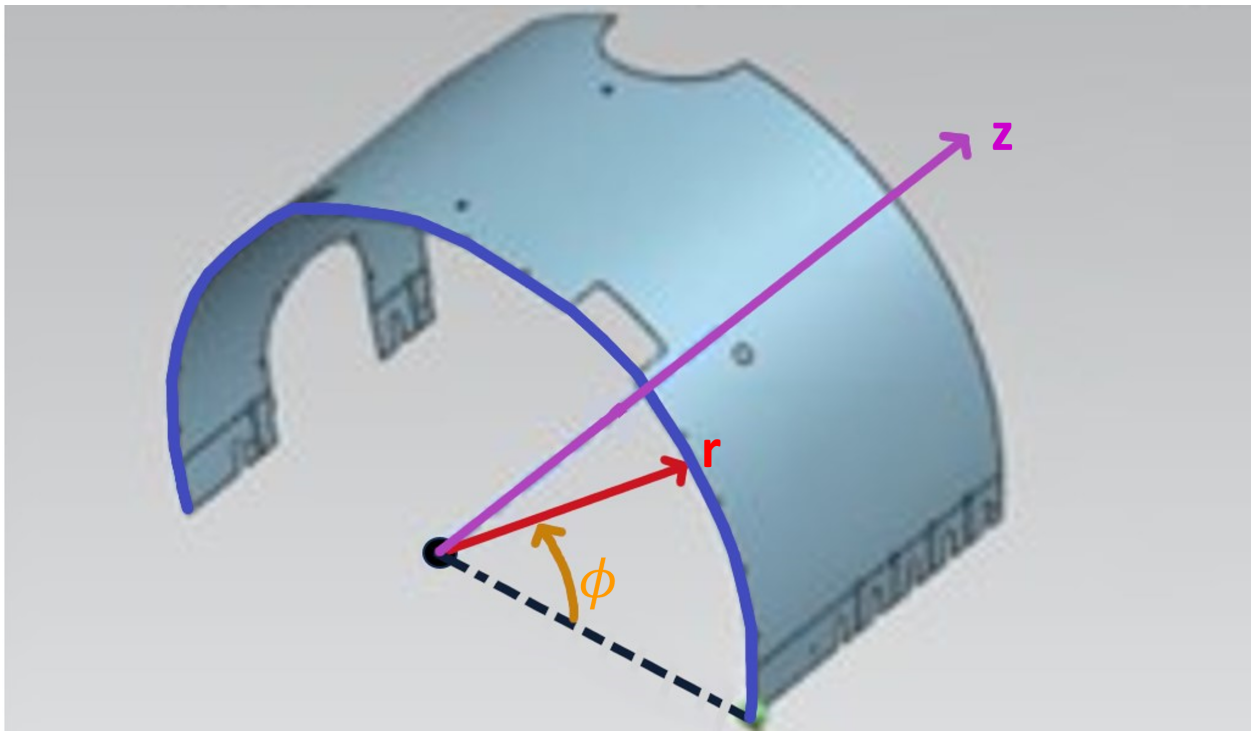

Figure 2.3: 3D model showing the upper thermal shield part Figure 2.2 represents (in blue) and the r,ϕ, and z axes of the model

Splitting the parts of the thermal shield into small sections gives rise to a dilemma. The sections need to be numerous enough to accurately analyze the thermal shield, however, not abundant enough that completing the derivations becomes near impossible. Even if a good balance were found, the completion of the derivations would be a herculean task.

Before beginning such a complex derivation, other solution methods should be considered. The method detailed above was the main method used for analysis before computers. The derivations are complex and numerous; however, a team of engineers could complete the analysis by working together. With the introduction of more advanced computing, more advanced tools also arose. Since the method above already divides the thermal shield into sections, using a program like Ansys Workbench that also divides a body into sections may be preferable. Computer programs like Ansys can divide the thermal shield into small sections

that would be impossible for people to finish deriving. However, a computer can easily maintain and solve the numerous amount of sections.

2.2 Ansys

Simulation programs, like Ansys Workbench, use the finite element method to convert complicated differential equation problems into a simpler system of equations problem. Typically, the amount of equations that result from this process also makes it nearly impossible to directly calculate a solution. Letting the computers solve the equations resulting from FEM is the quickest method to achieving results, beating out directly calculating either the FEM equations or the original differential equation.

The FEM process results in a ludicrous amount of equations since multiple equations are needed for each "finite element". During a finite element analysis (FEA), instead of evaluating the entire body at once, the body is split into many different finite elements. These finite elements can differ in shape and size, however, in the end, they must completely cover the original body. The finite element method trades complexity for abundance, instead of one very complex differential equation there are now many simpler equations. The governing equation for a FEM steady-state thermal analysis can be seen in Equation 2.7.

$$[q] = [K][T] \tag{2.7}$$

All three of the parameters inside of Equation 2.7 are matrices. The [q] matrix contains the heat flow information of all the finite element equations. The [K] matrix, typically called the stiffness matrix, contains the conduction and convection information of all the finite element equations. Lastly, the [T] matrix, typically called the temperature matrix, contains the temperature information of all the finite element equations. The boundary conditions

of the original body are also implemented in these matrices. Specifically, temperature and heat flow boundary conditions are used for this simulation. These boundary conditions are added by changing the values of the rows within the matrices, where the boundary condition is located.

Besides the conduction and convection values for the stiffness matrix, there are several unknowns in Equation 2.7. The current biggest unknown is the temperature matrix (T). The information located inside of the temperature matrix is the main goal of this simulation, with this information the temperature at each section of the thermal shield can be found. Unfortunately, many of the values inside of the stiffness matrix [K] are also dependent on the information inside of the temperature matrix. Finite element programs, like Ansys, excel in these situations. These programs can quickly and efficiently test a variety of different scenarios, using non-linear equations with stiffness matrices consisting of variables instead of constant values. The program will continue testing different scenarios until satisfactory results close to solutions of the original governing equations are found.

Using a finite element program, like Ansys, also has another important advantage, it makes the FEM process much more digestible. Instead of meticulously looking over and rearranging equations, the provided 3d environment makes setting up the FEA much simpler, faster, and intuitive. Material properties, boundary conditions, external forces, meshing properties, all these properties and more can easily be edited in programs like Ansys. Of course, these properties can also be edited when dealing with just the equations, however, Ansys explicitly visualizes those changes to the user. For example, if two sections of a body consist of two different materials, Ansys will visualize that difference by having the sections be different colors. FEM needs to be used due to the complexity of the thermal shield's thermal analysis. Ansys is still using FEM, however, the added interface Ansys provides makes the analysis much more understandable for both the user and their audience.

2.3 Ansys Setup

Ensuring that the simulation is set up correctly is a vital part of any finite element analysis. Any inaccurate boundary conditions or significant assumptions during the setup of the simulation can have detrimental effects on the accuracy of the results. For this reason, all of the data added to the simulation should be as close to realistic as possible but not burdensome to the calculation. This is especially crucial for a simulation at such low temperatures, like the thermal shield.

Ansys enables location or temperature-specific variables, such as thermal conductivity or convection coefficient, to be incorporated into the solution method. Luckily, Fermilab provided a data sheet containing the thermal conductivity values for the different materials used by the thermal shield at varying temperatures. This results in the sections furthest from the inlet point of the helium having higher temperatures. At such low temperatures, the thermal conductivity of a material can change significantly between a few degrees, as can be seen in Figure 2.4. Since the thermal shield is increasing in temperature, Ansys also needs to continuously update the thermal conductivity and convection coefficients of the different regions of the thermal shield for more accurate results. Continuously updating the conductivity and convection coefficients results in better accuracy since both values vary depending on the temperature. Since the thermal shield has been split into elements, Ansys can vary the different temperatures and properties of the elements until an acceptable solution is found. The different aspects of the thermal conductivity have been discussed, however, the convection occurring inside of the extrusion differs and has not been considered.

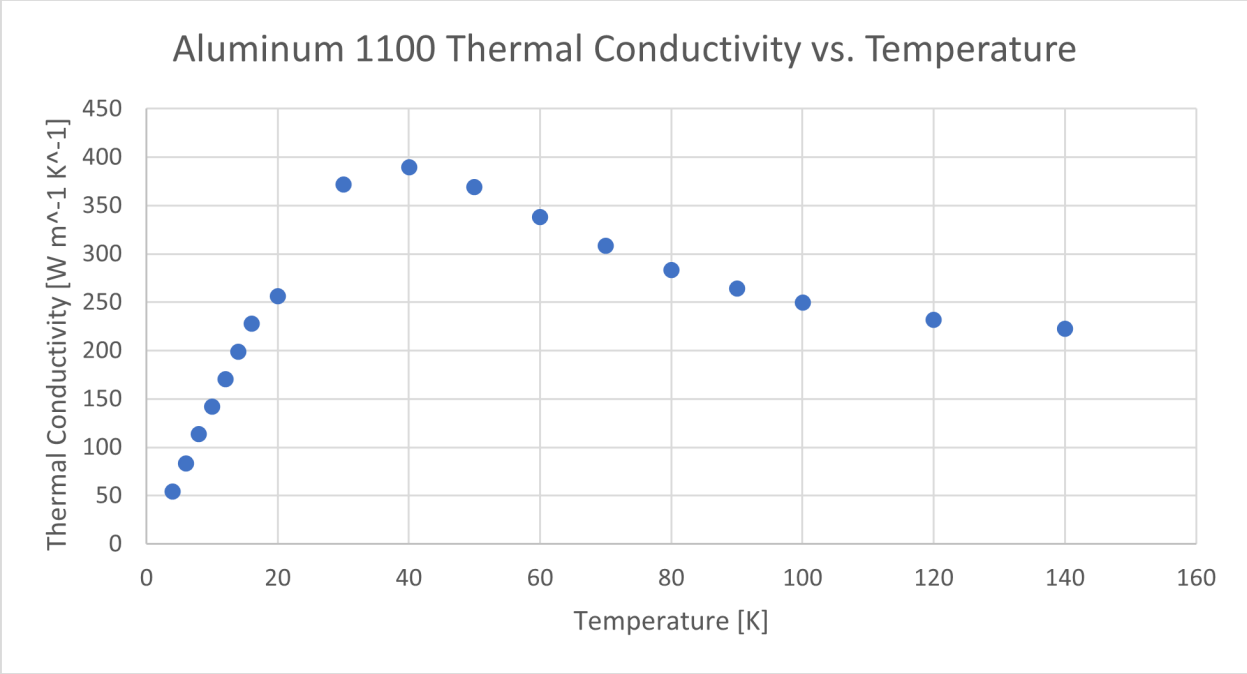

Figure 2.4: Plot showing how drastically the thermal conductivity of Aluminum 1100 can change at low temperatures [27]

2.3.1 Convection

$$q_{conv} = -hA\frac{dT}{dx} \tag{2.8}$$

Equation 2.8 is the governing convection equation for this analysis. The convective heat transfer (q_{conv}) is the product of the convection coefficient (h), the area (A), and the directional change in temperature ($\frac{dT}{dx}$). Equation 2.8 can be rearranged to find the needed temperature estimates.

Unlike thermal conductivity, there is no data sheet containing the convection coefficients for helium at different temperatures. These values are a bit more complex and have to be calculated with the specifics of the system in mind. The specific method used to calculate the convection coefficients for this analysis uses equations that only work for fluids in a pipe.

The thermal shield extrusion is just a pipe with some fins, so these equations will work for this scenario. Figure 2.5 visually shows how the extrusion compares to a pipe and some of the different heat transfer occurring on the pipe. Before derivation can begin, many different properties of helium need to be gathered. Density, viscosity, and thermal conductivity are just a few of the properties needed to begin the process of deriving the convection coefficient. However, even before these properties are gathered, it must be remembered that the convection value is dependent on the temperature only because many of the properties being gathered are also temperature-dependent. Many of these properties are not just temperature-dependent, many are also dependent on pressure. The first step to deriving the convection coefficients is deciding if the system is isothermal (constant temperature) or iso-

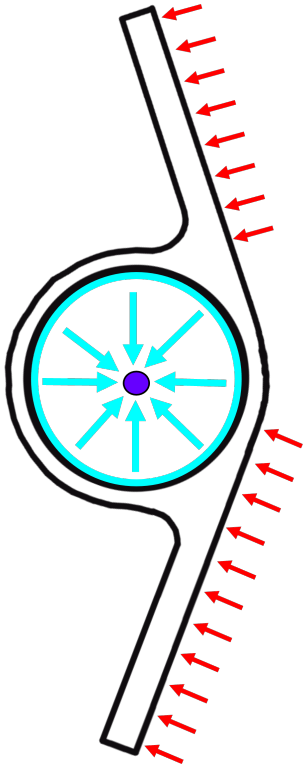

Figure 2.5: Sketch of the extrusion cross section; red arrows represent conductive heat transfer from the upper and lower thermal shields; the blue arrows represent convective heat transfer between the inner diameter of the extrusion and the helium heat sink (purple)

baric (constant pressure). The helium inside of the extrusion is kept at a constant pressure of 1.3 MPa, meanwhile, the temperature of the helium changes as it travels the extrusion, meaning the system is isobaric. With this information, the National Institute of Standards and Technology's (NIST) Chemistry WebBook becomes a phenomenal resource for finding the required data [28].

The NIST WebBook provides fluid properties at either constant temperatures or pressures for a variety of different fluids. The units of the different properties can also be changed depending on the user's preference. Figure 2.6 shows a screenshot of the data provided by the NIST WebBook for helium at 1.3 MPa. As can be seen from Figure 2.6, the NIST WeBook provides supplementary properties that are not required to solve for the convection coefficients. The properties that will be used from the NIST WebBook are the densities (ρ), the specific heat constants (C_p), the viscosities (μ), and the thermal conductivity values (λ).

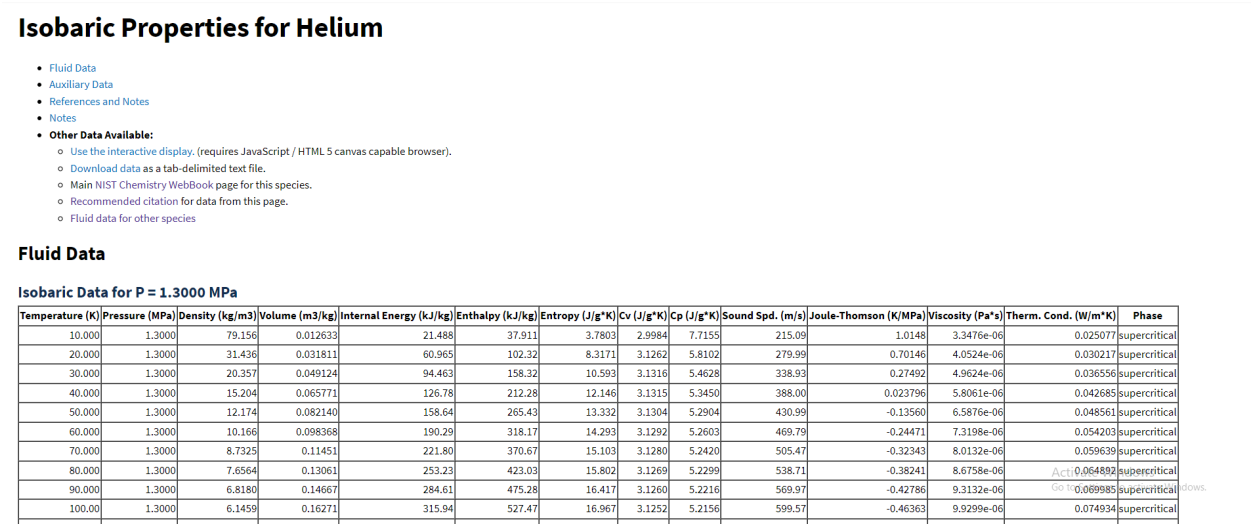

Isobaric Properties for Helium

- Fluid Data
- Auxiliary Data
- References and Notes
- Notes
- **Other Data Available:**
  - Use the interactive display. (requires JavaScript / HTML 5 canvas capable browser).
  - Download data as a tab-delimited text file.
  - Main NIST Chemistry WebBook page for this species.
  - Recommended citation for data from this page.
  - Fluid data for other species

Fluid Data

Isobaric Data for P = 1.3000 MPa

Temperature (K)	Pressure (MPa)	Density (kg/m3)	Volume (m3/kg)	Internal Energy (kJ/kg)	Enthalpy (kJ/kg)	Entropy (J/g*K)	Cv (J/g*K)	Cp (J/g*K)	Sound Spd. (m/s)	Joule-Thomson (K/MPa)	Viscosity (Pa*s)	Therm. Cond. (W/m*K)	Phase
10.000	1.3000	79.156	0.012633	21.488	37.911	3.7803	2.9984	7.7155	215.09	1.0148	3.3476e-06	0.025077	supercritical
20.000	1.3000	31.436	0.031811	60.965	102.32	8.3171	3.1262	5.8102	279.99	0.70146	4.0524e-06	0.030217	supercritical
30.000	1.3000	20.357	0.049124	94.463	158.32	10.593	3.1316	5.4628	338.93	0.27492	4.9624e-06	0.036556	supercritical
40.000	1.3000	15.204	0.065771	126.78	212.28	12.146	3.1315	5.3450	388.00	0.023796	5.8061e-06	0.042685	supercritical
50.000	1.3000	12.174	0.082140	158.64	265.43	13.332	3.1304	5.2904	430.99	-0.13560	6.5876e-06	0.048561	supercritical
60.000	1.3000	10.166	0.098368	190.29	318.17	14.293	3.1292	5.2603	469.79	-0.24471	7.3198e-06	0.054203	supercritical
70.000	1.3000	8.7325	0.11451	221.80	370.67	15.103	3.1280	5.2420	505.47	-0.32343	8.0132e-06	0.059639	supercritical
80.000	1.3000	7.6564	0.13061	253.23	423.03	15.802	3.1269	5.2299	538.71	-0.38241	8.6758e-06	0.064892	supercritical
90.000	1.3000	6.8180	0.14667	284.61	475.28	16.417	3.1260	5.2216	569.97	-0.42786	9.3132e-06	0.069985	supercritical
100.00	1.3000	6.1459	0.16271	315.94	527.47	16.967	3.1252	5.2156	599.57	-0.46363	9.9299e-06	0.074934	supercritical

Figure 2.6: Screenshot of data provided by NIST WebBook [28]

The following equations (Equations 2.9 – 2.13) demonstrate the rest of the process used to derive the helium's convection coefficients for the thermal simulation.

$$h = \frac{\lambda \ Nu}{d} \tag{2.9}$$

Equation 2.9 is the crux of this convection coefficient derivation. Equation 2.9 states that the convection coefficient is directly proportional to λ and Nu but inversely proportional to the pipe dimension (d). The thermal conductivity and the diameter are both already known values. Thermal conductivity values can be found via the NIST WebBook, meanwhile, the diameter is a constant value dependent on the geometry of the extrusion. The only value holding back the ability to solve this equation is the Nusselt number.

$$Nu = 0.023 Re^{4/5} Pr^{n} \tag{2.10}$$

The Nusselt number is a dimensionless number that is the ratio of convective and conductive heat transfer. Equation 2.10 expands on the Nusselt number ratio further through the Dittus-Boelter equation that incorporates Reynolds (Re) and Prandtl (Pr) numbers [29]. The NIST WebBook contains the parameters needed to solve the Reynolds and Prandtl numbers. The last component of Equation 2.10 that must be discussed is the "n" exponent. The value of n changes depending on whether the fluid is heated (n=0.4) or cooled (n=0.3). As the helium transverses the extrusion, it absorbs heat from the thermal shield, resulting in an n value of 0.4.

$$Pr = \frac{C_p \ \mu}{\lambda} \tag{2.11}$$

Equation 2.11 shows how the Prandtl number is derived. The parameters required to derive the Prandtl number are the specific heat at constant pressure (C_p), viscosity (μ), and thermal conductivity (λ). The Prandtl number is a dimensionless number that demonstrates

the ratio between momentum diffusivity and thermal diffusivity. All three parameters needed to derive the Prandtl number are located in the data gathered from the NIST WebBook, using said data the Prandtl number can be derived for helium at all the temperatures required.

$$Re = \frac{\rho \ w \ d}{\mu} \tag{2.12}$$

Equation 2.12 shows the derivation of the Reynolds number for flow in a pipe. The values for density (ρ), the characteristic linear dimension (d), and viscosity (μ) have all already been found.

$$w = \frac{\dot{m}}{0.25 \ \pi \ d^2 \ \rho} \tag{2.13}$$

Equation 2.13 shows how flow speed can be derived by rearranging the formula for mass flow rate. In order to solve for the flow speed in a pipe the mass flow rate ($\dot{m}$), the diameter of the pipe (d), and the density of the fluid (ρ) are required. The density (ρ) of the fluid changes depending on the temperature, the varying values are found via the NIST WebBook. Meanwhile, the diameter (d) is a geometric constant of the extrusion and the mass flow rate ($\dot{m}$) is a temperature-independent value that is known from the pumping inputs of the system. Equation 2.13 finishes this branch of the derivation, the Reynolds number needed back in Equation 2.10 can be derived.

$$h = \frac{(0.092\lambda(T) \ \rho(T) \ \dot{m})^{0.8} \ (C(T))^{0.4}}{\pi^{0.8} \ \mu(T)^{0.4} \ d^{2.2}} \tag{2.14}$$

The process detailed above results in Equation 2.14 which needs to be used to derive the convection coefficients. Since multiple convection coefficients at different temperatures are needed, this derivation needs to be carried out a multitude of times. Instead of deriving the convection coefficient by hand each time, all of the data and equations were moved onto an Excel spreadsheet. On this spreadsheet, values of the convection at different temperatures

can be calculated using Equation 2.14 and all of the fluid parameters that have been established. Using the spreadsheet to derive all the values allows for straightforward edits down the line. For example, for reasons that will be explained later in the paper, new convection coefficients needed to be calculated at different mass flow rates. With the spreadsheet, finding these new convection coefficients only required changing one column of the spreadsheet. Once the helium convection coefficients were calculated they were then also reduced by 15 percent to account for the error from the method used to calculate the convection coefficients. The reduced convection coefficient values can then be implemented into the Ansys simulation. In Ansys, when adding a convection boundary condition, the option of using either a scalar magnitude or a table is given. Using the table option, all of the calculated convection values can be implemented into Ansys. The implemented convection values work as a data-set for Ansys, which can then be used to find the appropriate convection coefficient depending on the temperature.

The helium inside of the extrusion is represented in the Ansys simulation by a 1D line element. Since the line element is 1D the temperature only changes in one direction, this direction being the path of the extrusion. Simplifying the helium down to a 1D element is acceptable since the temperature change in the radial direction will be minuscule compared to the temperature change along the path of the extrusion. The correct cross-section, mass flow rate, and conduction values were also added to the helium line element serving as the heat output boundary conditions. The mass flow rate only requires a geometry selection and a magnitude, meanwhile, the convection requires a geometry selection representing the fluid, another geometry selection representing the geometry that will be affected by the convection, and a magnitude. For the magnitude of the convection, the Ansys table setting is used instead of a single value.

2.3.2 Structures

The different structures and materials that make up the thermal shield are represented using imported and modeled components inside Ansys Workbench. The different components can then be assigned their appropriate properties. Most of the thermal shield geometry was imported into Ansys from the Fermilab made Siemens NX model located in TeamCenter under the ID of F10191721. Any components that were not imported were modeled in Ansys DesignModeler. Most of these components have complex geometries that would slow down the simulation. Due to their complex geometries, these components were simplified when modeled in Ansys DesignModeler.

Many of the components, once in the simulation, were converted from solid bodies to shell bodies. The switch from solid to shell bodies was done to lessen the computational strain of the simulation since many of the thermal shield components are suitable to being shell bodies. A shell body differs from a solid body by being 2D instead of 3D. Since the body is now 2D the solution time decreases drastically compared to a solid body, however, a shell body will only provide adequate results if the original geometry is "thin." A thin body is a 3D body that has two dimensions that are much larger than the other third dimension. While "ignoring" an entire dimension for multiple parts sounds like it would have detrimental effects on the simulation solution, it is a reasonable assumption. The thin dimensions of these bodies are so relatively small that the temperature gradient in that dimension barely changes. For example, a section of the upper thermal shield is going to have a much larger temperature change over the 1300 millimeters of its length than its 0.23% smaller 3-millimeter thickness. For this reason, limiting the analysis of the temperature gradient is a reasonable assumption that helps limit computational strain and has a minuscule impact on the simulation results. The effect of such an assumption can also be seen in Equation 2.6. If the method using

Equation 2.6 were to also treat the "thin" geometry as shell elements, all they $\frac{dT}{dr}$ terms within Equation 2.6 would be assumed to equal since there would be no thickness in the r-direction for the temperature to change. The $\frac{dT}{dr}$ terms going to zero make using Equation 2.6 easier since only the ϕ and z direction need to be evaluated.

Ansys Workbench also makes it easy to assign different material properties to the different bodies in the simulation. All that needs to be done beforehand is the creation and naming of a new material, in the Engineering Data section, and filling out the necessary material properties. For this thermal simulation, the most important data is the thermal conduction values of the material at different temperatures. For most of the materials used by the thermal shield, Fermilab provided a PDF containing the thermal data for the materials [27]. Constant thermal conduction values cannot be used since when dealing with such cold temperatures and highly conductive materials, the values can differ wildly depending on the temperature of the helium.

In summary, the theory and contextual details of this analysis have been addressed in this section. The governing equations, geometry, and both temperature-dependent and independent parameters required for the analysis were discussed and justified. A comparison between the different options for the analysis was also discussed. Subsequently, the methodology of the analysis will be discussed. The methodology includes a deeper look into the setup of the simulation and an elaboration of how the information from Chapter 2 is implemented.

CHAPTER 3

METHODOLOGY

3.1 Evaluation Criteria

Before starting a thermal simulation in earnest, it is essential to know the issues and specifications for the evaluation criteria. For this thermal analysis of the SSR1 thermal shield, it is crucial to ensure that no region of the shield exceeds 68 Kelvin, especially the regions around the current leads. The shield must remain under that temperature threshold due to the superconducting leads that provide electricity to the superconducting magnets inside of the thermal shield. Otherwise, the functional performance of the electric field inside of the SSR1 would not be sufficient.

Another important criterion that must be kept in mind is the cost of the thermal shield. The cost of the thermal shield must be kept as low as possible while still delivering performance metrics. The costs of the thermal shield include manufacturing, material, installation, additional components, operation, etc. In particular, it is crucial to minimize the combination of helium mass flow rate and inlet cold temperature; upfront investment costs can have a significant reduction in operation costs over the lifetime of the accelerator. Keeping the amount of helium used as low as possible saves money and resources by requiring less helium to be purchased and lessening the load on the cryoplant. If any additional components are designed, it is crucial to ensure the cost and time of addition are validated in a corresponding reduction in operational costs. Costs for additions are not just limited to financial costs. If an addition adds too much complexity or is impractical to install that would be another

reason why a design may be vetoed. The positives and negatives of any design must be thoroughly examined in both the short and long term before any decision on its fabrication is made.

3.2 Structures

A variety of different parts and sections make up the SSR1 thermal shield. The thermal shield is almost like a shell, protecting the more fragile components located deeper inside the cryomodule. The components farther inside of the cryomodule are more sensitive to temperature gradients. The thermal shield protects these sensitive components from the radiative heat transfer from objects at "high" temperatures above 70 Kelvin. Instead of reaching the inside components, the external high temperatures are occluded by the thermal shield, which is cooled via helium supplied at around 46 Kelvin. Every part of the thermal shield is vital for overall function, however, for this thermal analysis, some sections have a more significant impact than others. The four components with the largest impact on the system are the extrusion carrying the liquid helium, the upper shield, the lower shield, and the thermal straps. However, for thoroughness, it is best to provide descriptions and summaries of each section of the thermal shield. Each of these sections was imported into Ansys from the official Siemens NX model of the thermal shield, and implemented into the steady-state thermal model produced.

A majority of parts of the thermal shield model are 2D shell bodies. The only parts that remained 3D solid bodies were the extrusion, the welds connecting the extrusion to the upper and lower shield, and some thermal strap representations added to the simulation. Due to the mix of 2D shell elements and 3D solid bodies in the simulation, many interesting interactions occur between the different sections. In the simulation, there are connections

between solid bodies and solid bodies, shell bodies and shell bodies, and between solid bodies and shell bodies. Figure 3.1 shows a cross-section of the solid body extrusion.

The solid body to solid body connections all revolve around the extrusion. The different sections of the extrusion needed bonded contacts between each adjacent section to best represent the physically connected extrusion. The connections between the welds and the extrusion are also connections between a solid body and another solid body. These solid body to solid body connections are basic Ansys connections done in most simulations connecting one face of a solid to another face on a different solid body.

The connections between two different shell elements are a little more complicated. Most of the shell body to shell body connections are not between faces of the shells' geometry, like the solid body to solid body connections. Instead, connections between two shell bodies typically involve either two curves (1 from each shell body) or one curve and one shell face (with a pinball radius). When adding a contact involving the face of a shell body, the specific face must be selected in the options for the contact. If the option is left on

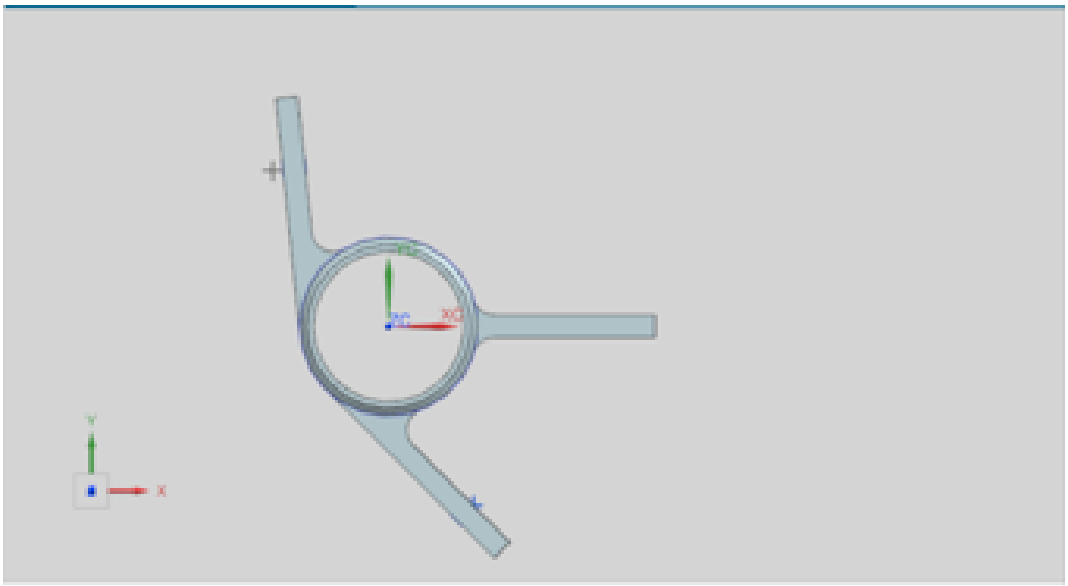

Figure 3.1: Cross section of the extrusion (F10151355)

"Program Controlled," there is a more than likely chance that Ansys will pick the wrong face of the shell body, misrepresenting the contact. A contact between the face of a shell body and an edge can also be computationally inconsistent, adding a pinball radius can help mitigate connection issues [30]. The added pinball radius helps ensure the elements around the connection point are affected by the contact. This type of contact is used since most of these connections are achieved via some sort of fastener. Only the area around the hole for the fastener will have direct contact between the two bodies.

The connection between a solid body and a shell body is the most complex of all the connection types in the simulation. This connection is only seen when attempting to represent the connection between the welds and either the upper or lower shield. Triangular solid bodies were used to represent the welds, these bodies were then "connected" to the thermal shield [25]. Different methods of connecting the welds were tested to best simulate the connection. The combination of merged topology and a node merge resulted in the best results. The merge topology option was selected in DesignModeler when the welds were modeled. This topology merge works as a bonded contact between the two surfaces. Meanwhile, a node merge was used between edges on the shield called fingers, and the face of the weld in contact with that finger edge. A visual example of the node merge setup can be seen in Figure 3.2. Figure 3.2 also shows the edge of the thermal shield finger at the center of the weld. This detail can be better observed in Figure 3.3. The fingers were positioned at this location to better represent how the physical weld would act. The node merge method was used instead of the simpler method of using bonded contacts since it resulted in more accurate results when the geometry of the welds was changed. The simpler solution of using bonded contacts between the thermal shield fingers and the welds most likely struggled due to the interactions between the mesh of the solid body extrusion and the mesh of the 2D shell body thermal shield finger edges.

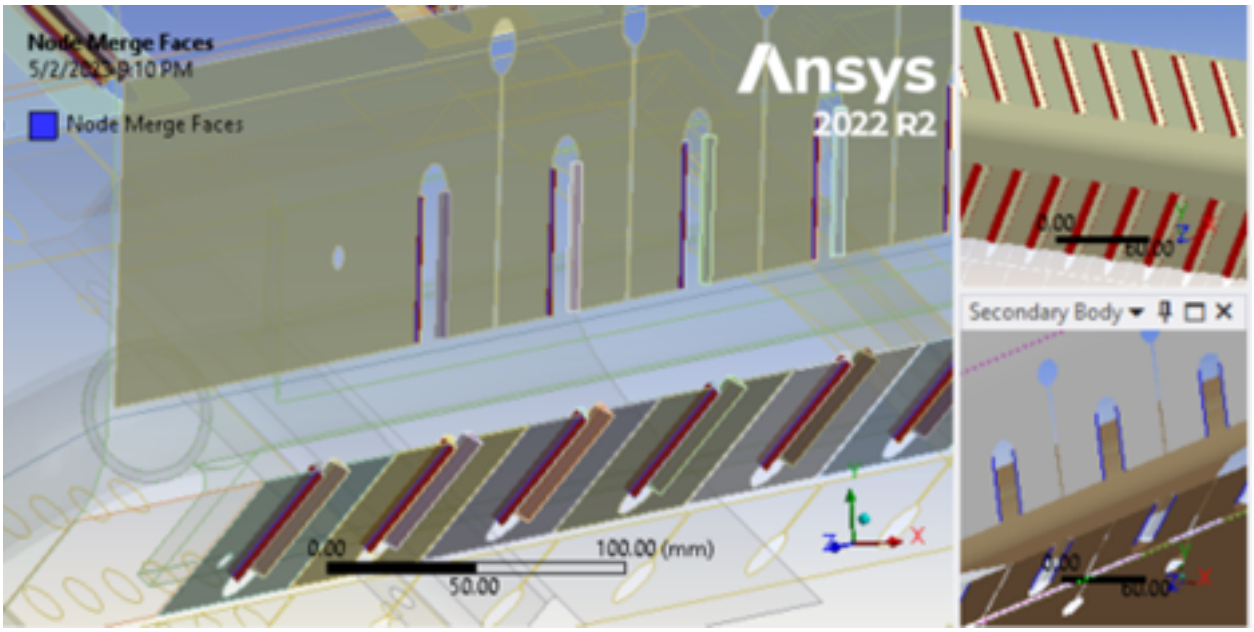

Figure 3.2: Set-up of the node merge between the lower thermal shield and the welds (blue: contact edges; red: contact faces)

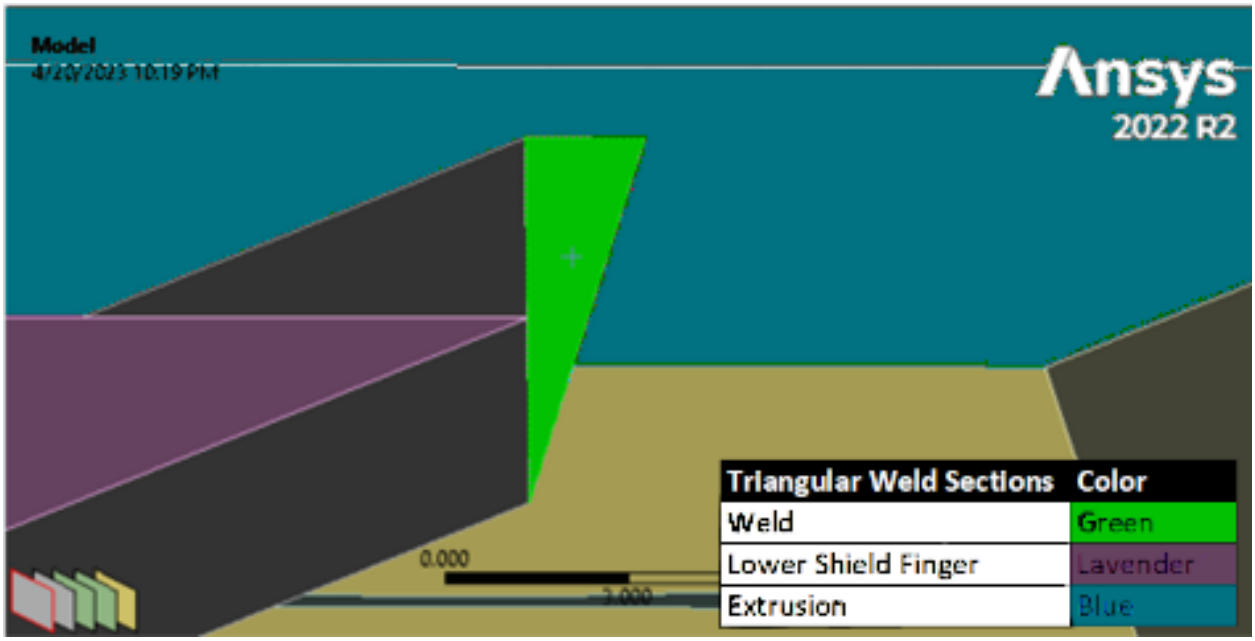

Figure 3.3: Triangular weld representation highlighted in green, the base of the weld is in contact with the extrusion via shell-to-solid contact, the vertical section is in contact with the lower thermal shield via solid body-to-solid body contacts

3.2.1 Extrusion

From a thermal standpoint, the extrusion is the most fundamental source of cooling within the thermal shield. The extrusion can best be thought of in five parts. In order from helium inlet to helium exit, these parts are the first short straight extrusion with two fins, the first elbow section, the only long straight extrusion with three fins, the second elbow section, and the second short straight extrusion with two fins. All five sections of the extrusion can be seen in Figure 3.4, with color-coded descriptions yet all are still fabricated from 6063 aluminum. The main purpose of the extrusion is to contain and circulate the helium throughout the thermal shield. The extrusion is also a crucial component for changing the temperature of the overall thermal shield. Changing either the mass flow rate or the inlet temperature of the helium entering the extrusion can drastically change the overall temperature of the entire

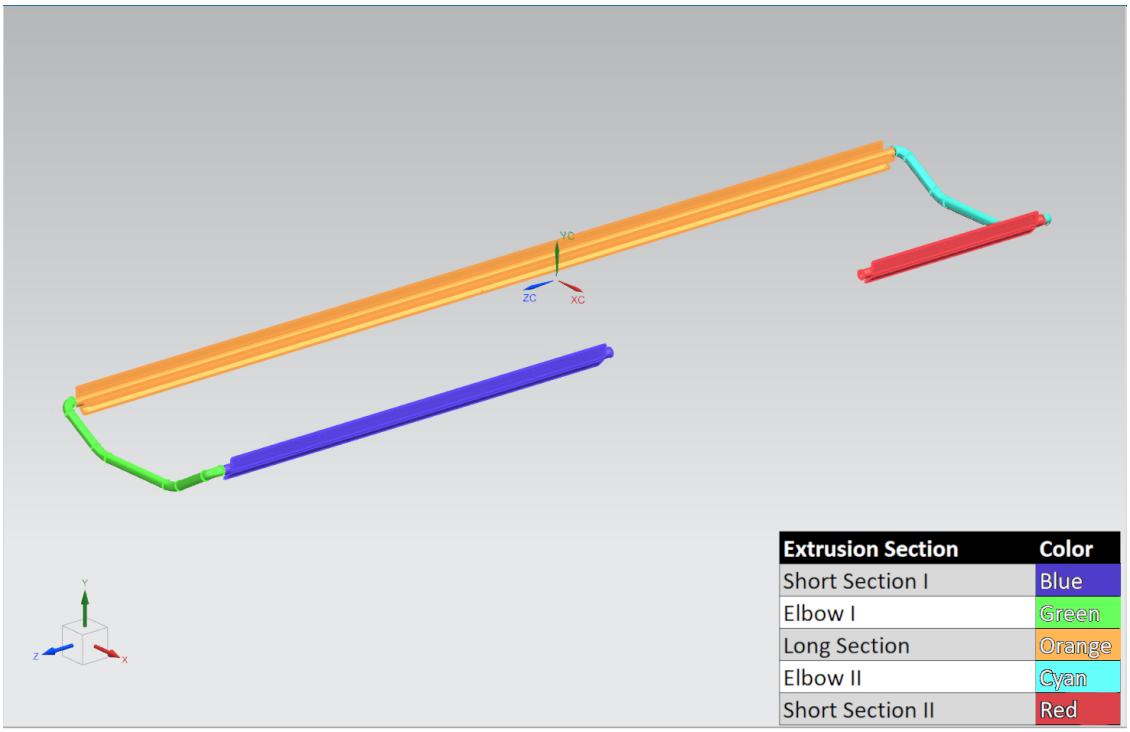

Figure 3.4: Labeled CAD model of the extrusion (F10147249)

thermal shield. The impact the mass flow rate and inlet temperature of the helium have can be observed in Equation 2.8. Changing the mass flow will change the amount of helium inside of the extrusion and affect the convection coefficient in Equation 2.8. Changing the inlet temperature will also have a drastic effect on the convection coefficient in Equation 2.8 since many of the parameters needed to calculate the convection coefficient are dependent on temperature.

3.2.2 Shell pieces

Figure 3.5 shows one section of the upper thermal shield, meanwhile Figure 3.6 shows one section of the lower thermal shield. The upper and lower thermal shield sections make up most of the thermal shield surface area and volume. All sections of the upper and lower thermal shield are made from aluminum 1100 and are situated axially from each other. This axial placement of the different shield sections ensures the thermal shield encompasses all of

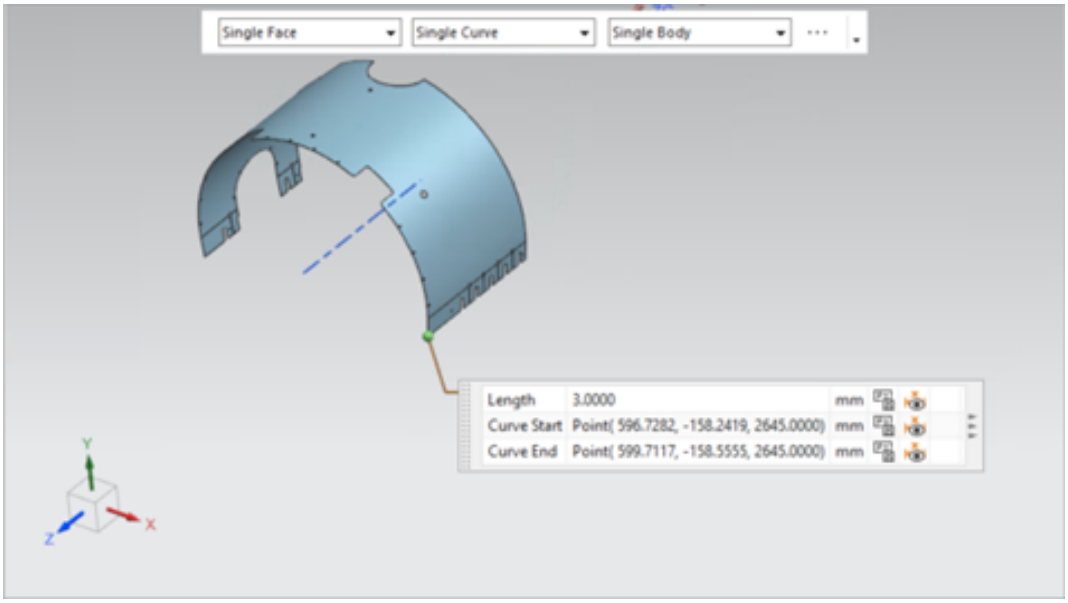

Figure 3.5: Section of the upper thermal shield (F10191726)

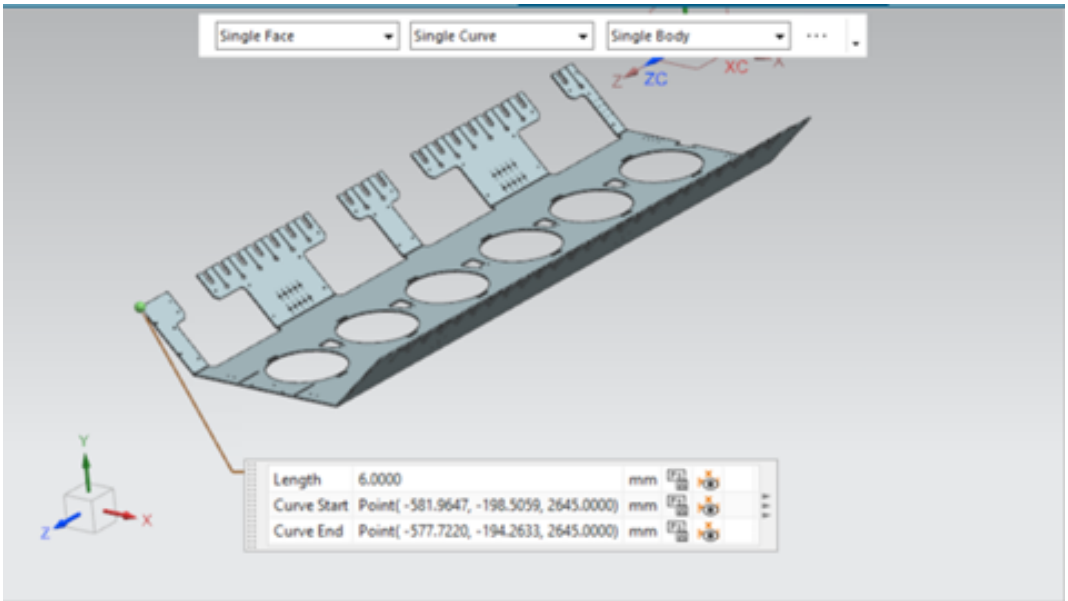

Figure 3.6: Section of the lower thermal shield (F10147253)

the sensitive components deeper in the cryomodule and protects them from any external high temperatures. All sections of the upper and lower thermal shield are represented in Ansys as 2D shell elements. The thin dimension of these shields is their thickness. All sections have thicknesses in the single-digit millimeters, meanwhile, the lengths and widths of the thermal shield sections can exceed one meter. All sections of the upper and lower thermal shield also have regions called "fingers" which were specifically designed to be the weld areas between the shield and the extrusion.

The upper thermal shield is split into 5 sections, all with a thickness of 3 millimeters. Each section of the upper thermal shield is circular in shape with flat sides. Figure 3.7 gives a clear visual of the profile of one section of the upper thermal shield. The upper thermal shield sections are all open semi-circles with radii of 1220 mm. At the ends of the semi-circles linear sections at an angle are added. The added linear sections are the areas where the weld fingers are added. Each section of the upper thermal shield also has many different openings for components like covers and ports. Each section of the thermal shield has openings in

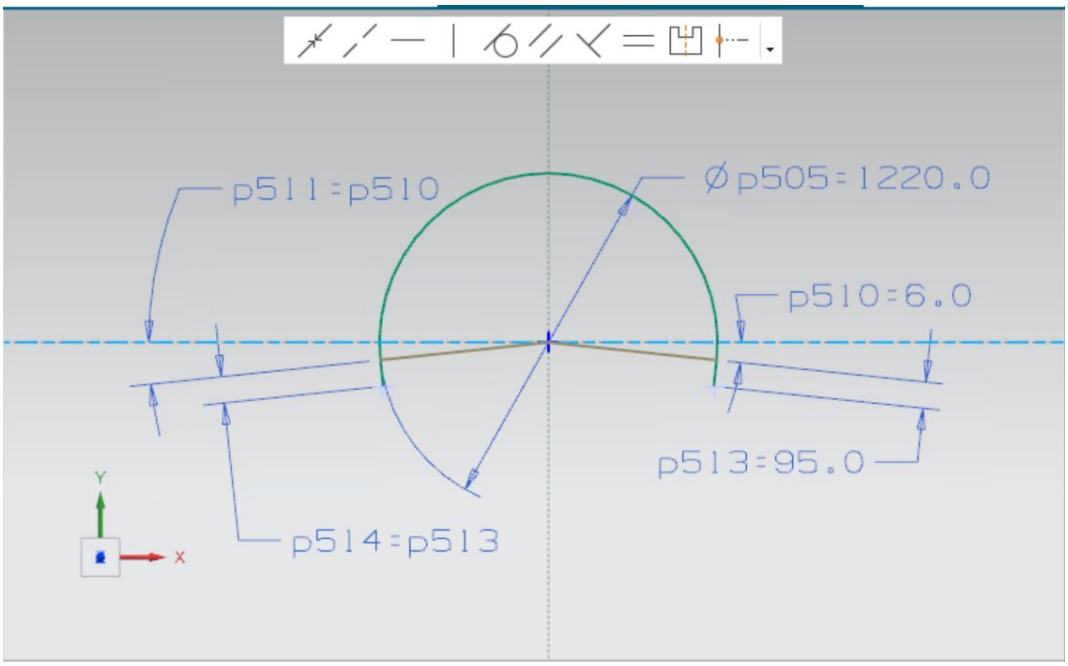

Figure 3.7: NX sketch of upper thermal shield section (F10191726)

different locations to accommodate the access points for the specific components that need to penetrate the thermal shield at that location. For example, the two upper shield sections located at the center of the thermal shield differ from the other sections since they need to interface with the top port. The openings on the upper thermal shield are less defined, and more compound shapes (semi-circles on rectangles compared to the openings on the lower thermal shield.

The lower thermal shield is split into 2 sections, each of which has a thickness of 6 millimeters. Unlike the more circular shape of the upper thermal shield sections, the lower thermal shield has more of a trough shape. Figure 3.8 shows the sketch used in NX to model a section of the lower thermal shield. The two sections of the lower thermal shield are connected by square brackets at four points along the center of the thermal shield. This connection was represented in the simulation by adding 4 bonded contacts to each edge of the lower shield in the same location and the same size as the square/rectangular brackets.

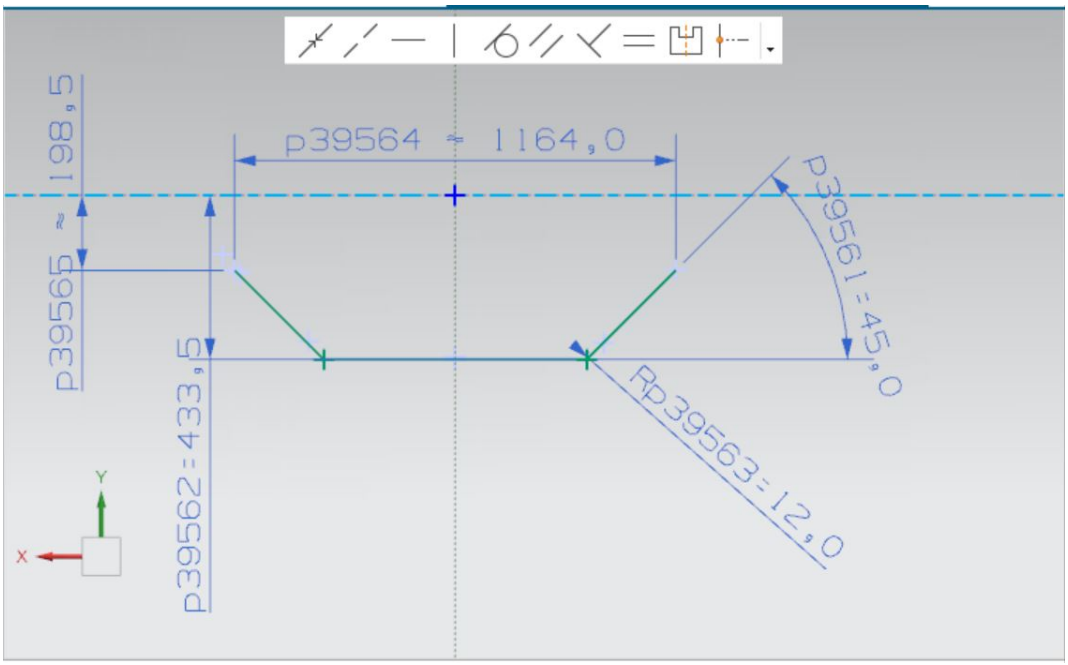

Figure 3.8: NX sketch of lower thermal shield section (F10147253)

Figure 3.9 shows all four of the lower shield connections in the CAD model. Meanwhile, Figure 3.10 shows a comparison between the connection in the CAD model and the connection in the simulation. The contact for the lower shield connection was accomplished by splitting the corresponding edges of the lower thermal shield. The edges were split to match the approximate connection length of the original square brackets. Some of the split edges were also extended to ensure the bonded contacts functionality, these extensions can be seen in Figure 3.10b. The openings on the lower thermal shield sections are more rudimentary geometries for pass-through compared to the openings on the upper thermal shield sections. For example, the openings for the support posts and tuner access ports are complete circles and rectangles.

The five sections of the upper thermal shield are not connected to one another. The structural support and most important thermal connection on the sections of the upper thermal shield comes from the connection to the extrusion. Many of the upper thermal

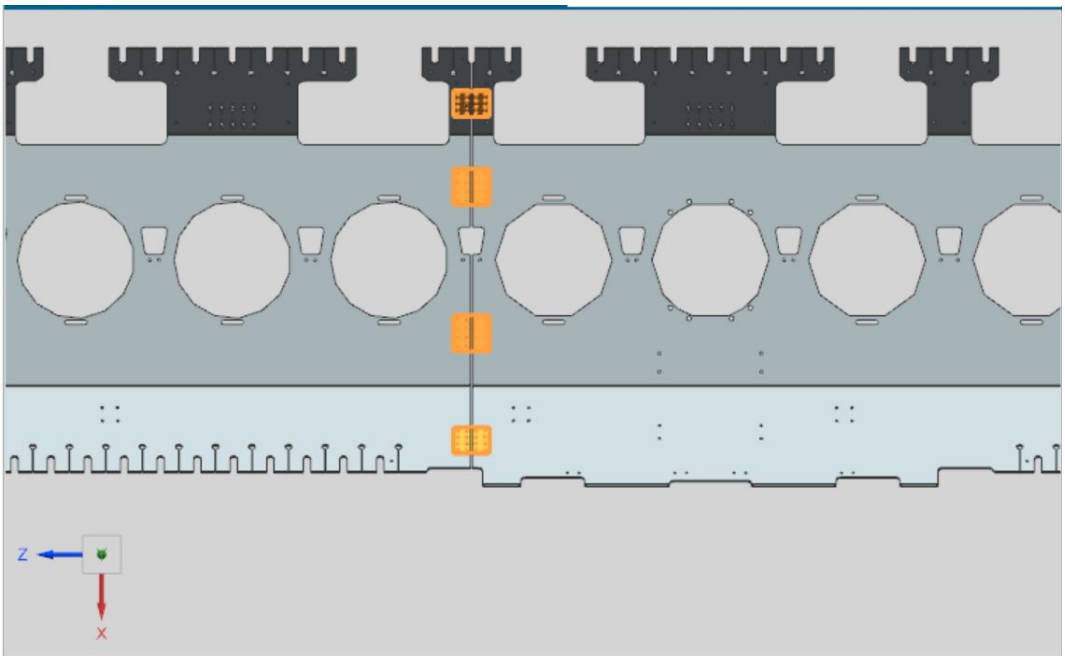

Figure 3.9: All four lower shield connection brackets (F10147249)

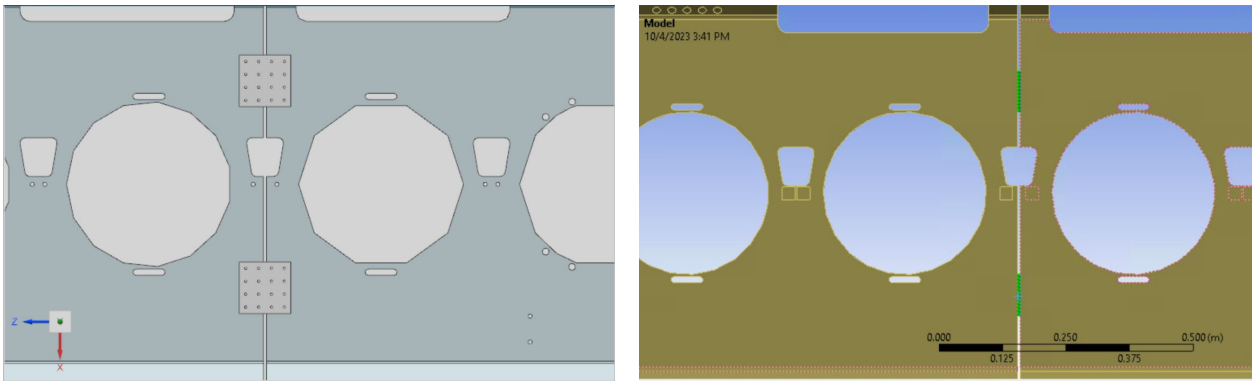

(a) (b)

Figure 3.10: Connection between the two lower thermal shield sections (a) lower shield connection in NX model (F10147249); (b) Lower shield connection in simulation

shield sections are also connected to ports of the thermal shield and have covers connected to them. The two sections of the lower thermal shield are connected at three points, however, their connection to the extrusion is far more impactful. The lower thermal shield also has connections to ports and covers of the thermal shield. The side port and the end caps of the

thermal shield are connected to sections of both the upper and lower thermal shield, creating different heat paths away from the extrusion.

3.2.3 Covers and Ports

The upper and lower thermal shield sections also have a variety of other thermal shield components attached throughout their span. These components include different covers and ports which all have purposes in the overall cryomodule. Figure 3.11 shows the location of the three different types of covers on the thermal shield assembly.

The three cover types shown in Figure 3.11 are all made from aluminum 1100, all have a thickness of 3 millimeters, and are all represented as shell elements in the simulation. While the covers do not have the largest impact on the thermal simulation, adding the covers is

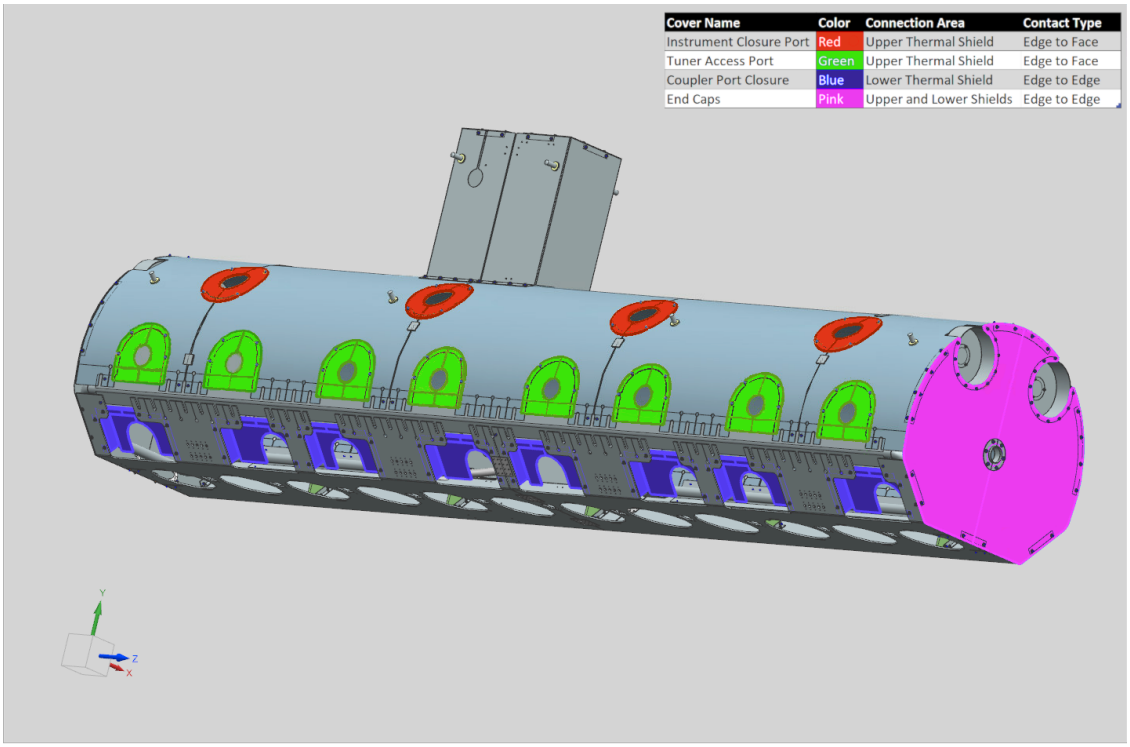

Figure 3.11: All three types of covers color coordinated (F10191721)

simple and provides more accurate results. When added to the model, bonded contacts were applied to the covers to mimic their contact with the rest of the thermal shield. Depending on the type of connection used on the cover two different applications of bonded contacts were used. Figure 3.12 shows the edge-to-edge bonded contact used, meanwhile, Figure 3.13 shows the face-to-edge bonded contact used. Figure 3.13 also shows why two different

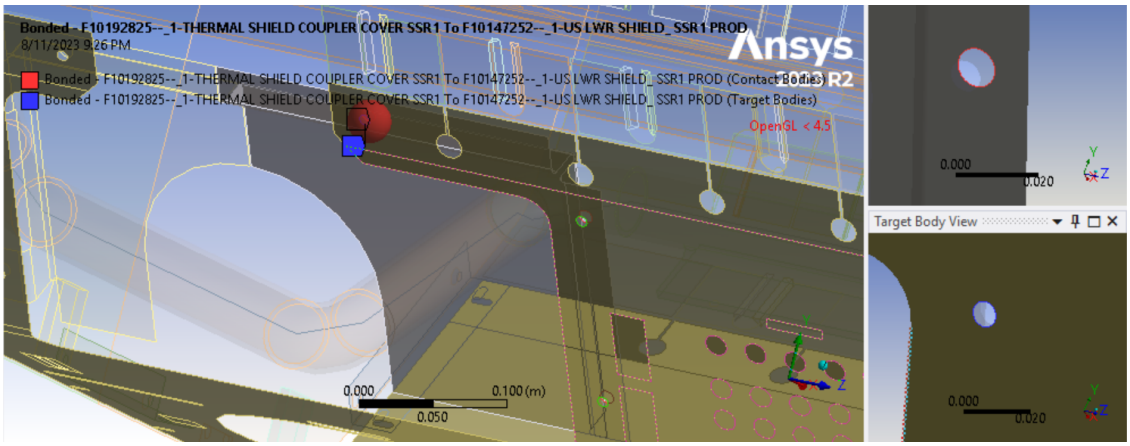

Figure 3.12: Edge to edge bonded contact

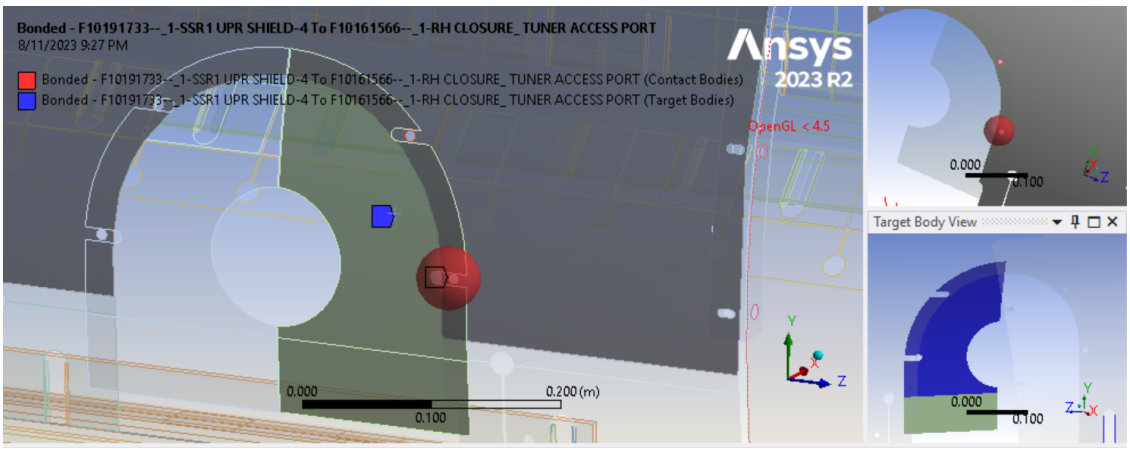

Figure 3.13: Edge to face bonded contact

types of bonded contacts needed to be used. The edge-to-edge bonded contact works great for connections where two circular edges are coincident, however, as Figure 3.13 shows this is not always the case. In situations like Figure 3.13 a bonded contact between a circular edge

and a planar face is used. A reasonable pinball region radius is then also added to assure an accurate contact region. The instrument closure cover and the tuner access port cover both used the face-to-edge bonded contact. Meanwhile, the coupler covers make use of the edge-to-edge bonded contact. There are 4 pairs of the instrument closure port covers and 8 pairs of the tuner access port covers which are all attached to the sections of the upper thermal shield. There are also 8 pairs of the coupler covers which are all attached to the sections of the lower thermal shield.

Another set of similar components that make up the model are the thermal shield end covers, the side port, and the top port. Each of these components is made from aluminum 1100 and are all 3 millimeters thick. All three of these sections also have similar purposes, they are used to protect components inside of the thermal shield. The end caps finish the job started by the upper and lower thermal shield sections of enclosing the beamline, the side port protects the entrance and the exit of helium used by the thermal shield, and the top port protects components like the transducer and heat exchanger. All three of these components and their location on the thermal shield can be seen in Figure 3.14. The top port, side port, and end caps also all make use of the edge-to-edge bonded contact.

The side and top ports both have circular edges that match up with their connection location on the thermal shield leading to contacts similar to Figure 3.12. The thermal shield end caps also use the edge-to-edge bonded contact, however, they also use imported brackets for the connection. These brackets were imported along with the thermal shield model and represent how the end caps will be connected on the physical cryomodule. These brackets, which can be seen in Figure 3.15, connect the end caps to both the upper and lower thermal shield.

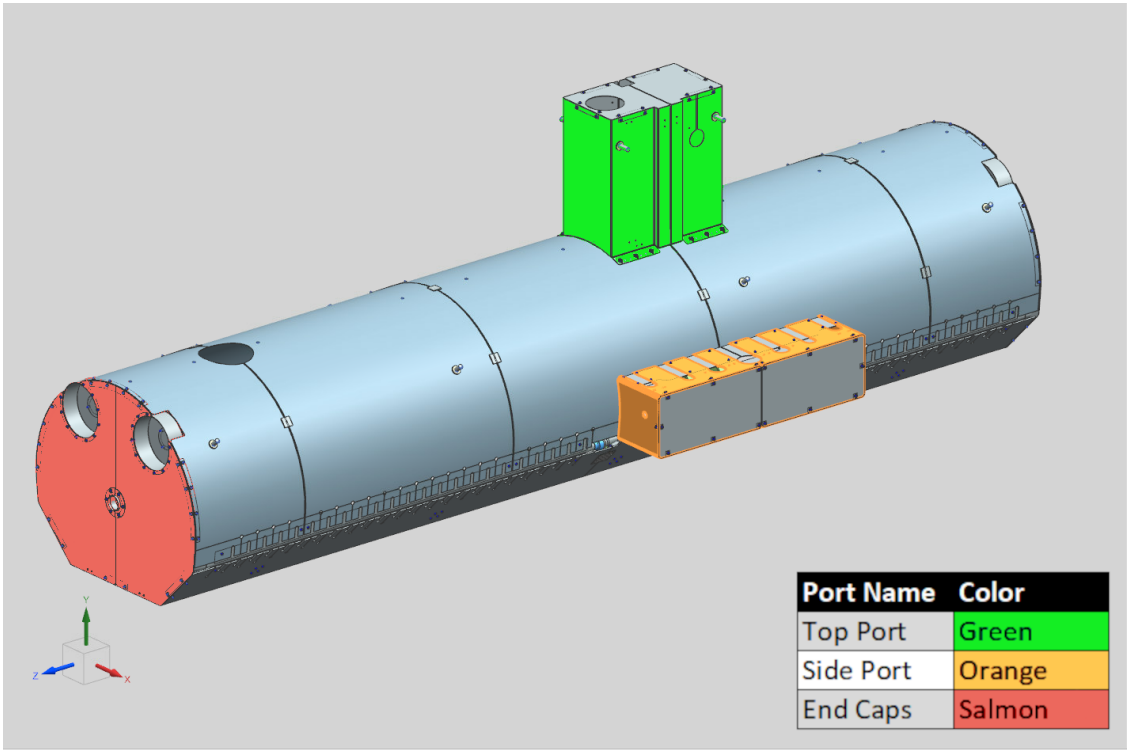

Figure 3.14: Graphic showing the locations of the top port, side port, and end caps (F10191721)

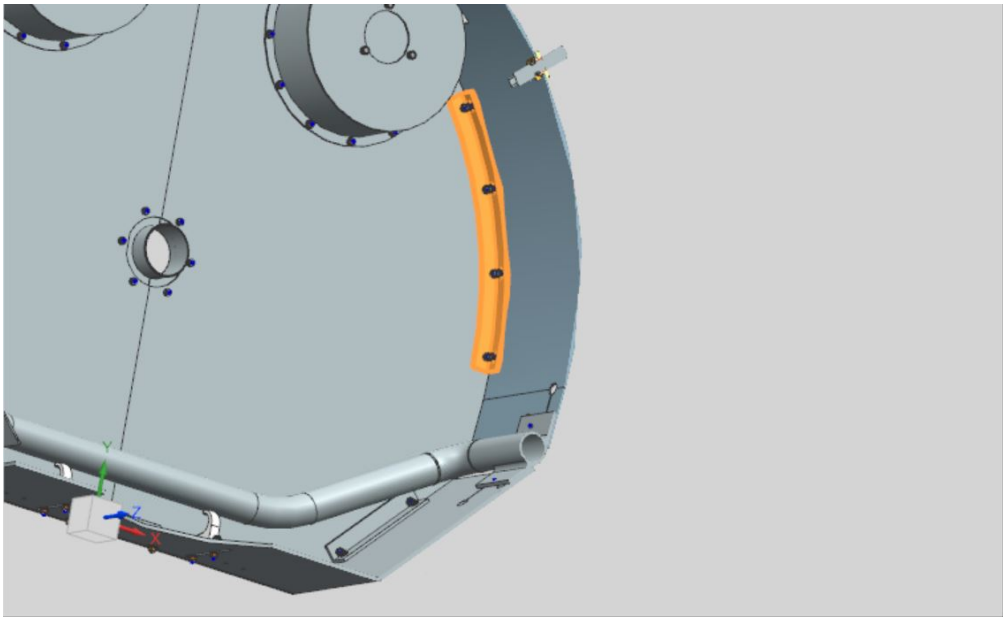

Figure 3.15: Thermal shield bracket (F10191721)

3.2.4 Thermal Straps

A very important component of the overall thermal efficiency is the multiple thermal straps located along the thermal shield. The thermal straps are used to better disperse the heat on the thermal shield. The thermal straps are made from oxygen free high conductivity (OFHC) copper with a residual resistance ratio (RRR) of 50. The residual resistance ratio measures the electrical resistance at 295 Kelvin vs. the resistance when submerged at 4 Kelvin. Adding the thermal straps into the thermal simulation directly from the CAD model would slow down and complicate the model drastically. This is because of the complexity of the thermal strap model compared to the rest of the thermal shield, and since the thermal straps would most likely have to be kept as solid bodies. Instead of importing the thermal straps directly from the CAD model, two different, less computationally intensive, methods of representing the thermal straps were used. The significant differences between the connection types of the thermal straps resulted in the need for the two thermal strap representations.

The first connection type of thermal strap is a thermal strap that connects a section of the thermal shield to another component within the cryomodule that is not part of the thermal shield. This kind of connection is mostly used to cool down components in the cryomodule and will be discussed further during Section 3.3. This thermal strap representation makes the area of the thermal shield where the thermal strap is connected into an "imprint." An "imprint" is a method of differentiating a section of a body using a pre-made curve. The pre-made curve in this scenario is the rectangular connection area of the thermal strap on the thermal shield. Figure 3.16 helps in clarifying this process. A heat flow is then applied to the imprinted area. This heat flow is equivalent to the heat load transferred to the thermal shield from the other object connected to the thermal strap. Since it is assumed the thermal straps are excellent at transferring heat, it can also be assumed that the calculated heat load

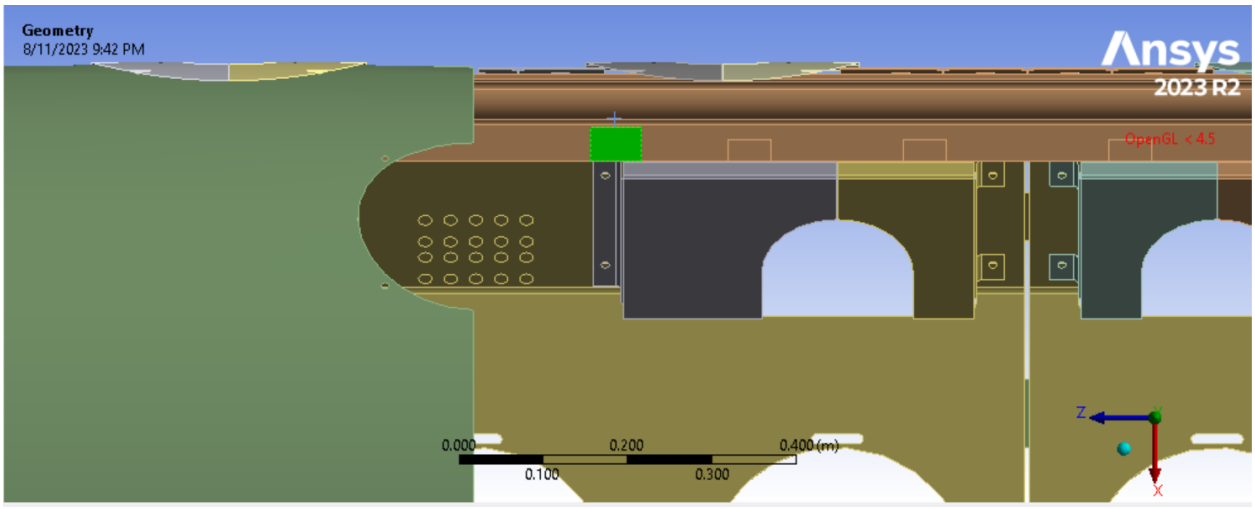

Figure 3.16: Images showing an imprint on extrusion

values will not change while being transferred by the thermal strap. This set of thermal straps was modeled in this way since the components the thermal straps connect to are not included in the model. The assumptions made can also be justified since the assumption does not result in a substantial temperature difference. The assumption slightly overestimates the heat load, which is preferable to underestimating the heat load.

The second type of thermal strap connection simulated in the model is a thermal strap connecting one section of the thermal shield to another section of the thermal shield. Typically, this type of thermal strap connects hotter regions of the thermal shield to colder regions of the thermal shield. Connecting these two locations helps disperse the heat. This type of connection can be physically modeled in the simulation since, unlike the previous scenario, both connection points exist in the model. This simulated thermal strap also makes use of imprints from the rectangular connection areas of the thermal straps. One of these rectangular areas is chosen and a rectangular extrusion with the same dimensions of the thermal strap is added at the center of the imprint. The extrusion at the center of the imprint simulates the thermal strap's copper braids. The area and extrusion length of the representation are kept as similar to the actual thermal strap as possible to provide a good

representation. This extrusion is also assigned the same material properties as a real thermal strap, including a varying thermal conductivity depending on the temperature. In order to ensure good contact, a bonded contact is added between the thermal strap imprint and the face in contact with the thermal shield. In order to simulate the connection between the other end of the thermal strap and the other section of the thermal shield a coupling boundary condition is used. A coupling boundary condition causes the temperatures of all the nodes on the selected faces to take the same value, which is tracked by only one temperature degree of freedom. The coupling boundary condition is used instead of importing or modeling the actual connection since it keeps the geometry simple. In total, there are 9 thermal strap extrusion representations, there is 1 connecting the top port to another section of the top port, there are 4 connecting the sections of the lower shield to the end caps, and there are 4 connecting the side port to the lower thermal shield. Figure 3.17 shows the thermal strap extrusion representation at the top port.

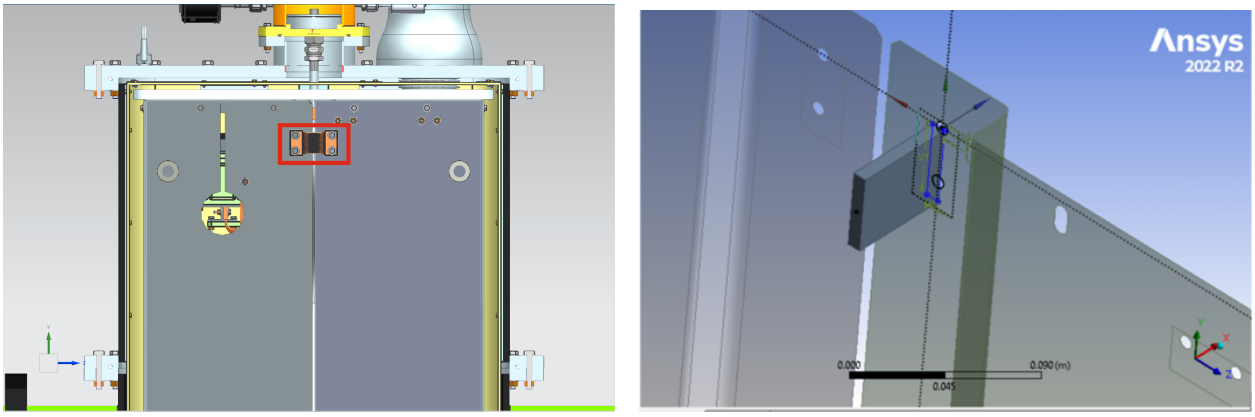

(a) (b)

Figure 3.17: Top port thermal strap comparison (a) thermal strap connecting one section of the top port to another (F10191721); (b) representation of top port thermal strap in the simulation

3.3 Heat Sources

Table 3.1 shows a spreadsheet containing data on the different heat sources inside the SSR1 cryomodule [31], [32]. This thermal analysis uses the values under the High-Temperature Thermal Shield (HTTS) column since those are the heat loads that act on the thermal shield being analyzed. Using the data from the spreadsheet, correct heat load values can be applied in the simulation in the appropriate location. At first glance, it may be confusing why some heat sources are listed twice on the spreadsheet. These heat sources are listed twice since they technically have two different heat loads depending on the status of the beamline. These heat sources have both a static and dynamic heat load. The

Table 3.1: Spreadsheet containing data on the heat sources [31]

	Each Unit (W)	#	Total (W)
	HTTS		HTTS
Input coupler (static)	12.30	8	98.40
Input coupler (dynamic)	1.20	8	9.60
Support post & cavity post & solenoid post	1.94	12	23.25
Thermal shield	49.78	1	49.78
View ports	1.36	4	5.44
Relief line	1.10	1	1.10
Current leads (static)	10.70	4	42.80
Current leads (dynamic)	11.50	4	46.00
Pressure transducer line	1.37	1	1.37
HX support	1.06	1	1.06
Cryo port	7.17	1	7.17
Instrumentation	1.58	-	1.58

static heat load is always present, meanwhile, the dynamic heat load is only present if the beamline inside of the cryomodule is also operating. Since the dynamic case will always deal with more heat, compared to the static case, the dynamic case is the focus of this thermal simulation. However, the heat loads were added in such a way that the simulation could easily be changed to examine the static case.

Many of the heat sources acting on the thermal shield have thermal straps connecting the heat source to the thermal shield. The heat sources that connect to the thermal shield via thermal straps include the couplers, the support posts, the relief line, the pressure transducer, the HX support, and the instrumentation to an extent. For these cases, the area where the thermal strap connects to the thermal shield is imprinted onto the model, and the heat load is applied to that area. The heat load is applied using the heat flow boundary condition with the values from Table 3.1 as the magnitude. When applying the heat load it is crucial to keep certain things in consideration. For starters, the values under the HTTS column typically refer to only one component of the overall heat source. For example, the magnitude listed for the support post heat source is 1.94 Watts, this value is for only one out of the twelve support posts in the model. In Figure 3.18 it can be seen that one of the support posts has two thermal straps connecting it to the shield. Figure 3.18 also shows the imprint area of those thermal straps on the shield. The 1.94 Watt heat load is applied and shared between those two imprint areas seen in Figure 3.18. Since there are twelve different support posts in the cryomodule, 12 different heat loads were created for each support post.

The radiation heat load in Table 3.1 represents the heat radiation on the thermal shield from the components outside of the thermal shield region. This heat source is labeled ”thermal shield” in Table 3.1 and is applied differently from the other heat loads. The radiation heat load is applied using the heat flux boundary condition on every outside component of the thermal shield. Outside component referring to any part of the thermal shield not enclosed by another section of the thermal shield, this includes both the upper and lower

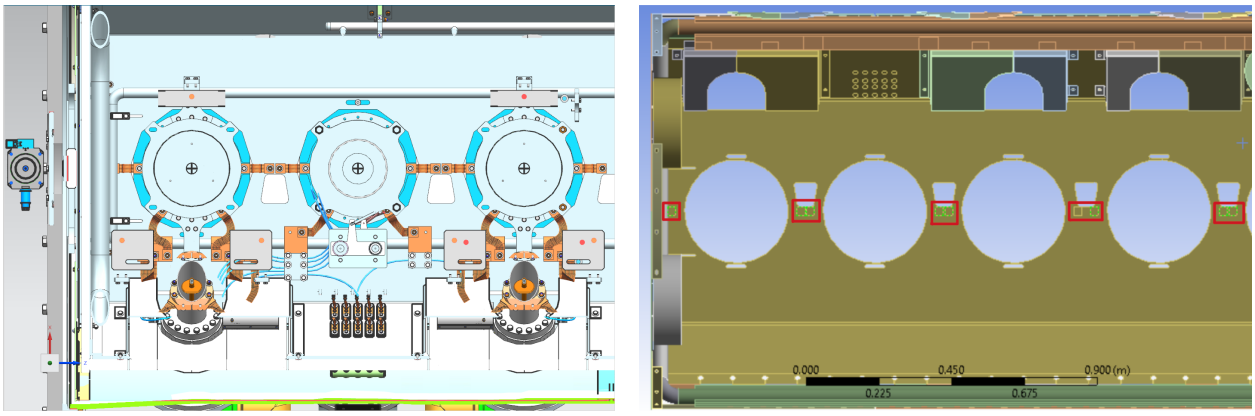

(a) (b)

Figure 3.18: Support post heat load (a) Picture of support post CAD with two thermal straps (F10142933); (b) Support post heat load example in simulation

shield, the covers, and the ports. A magnitude of 1.5 $\frac{W}{mm^2}$ was used when applying the heat load, which can be seen in Figure 3.19. Technically, there is also a "negative" radiation heat load coming from the colder internal components. However, this value is insignificant enough to ignore. The magnitude used for the radiation heat load was found by Fermilab engineers using previous experience working with cryomodules.

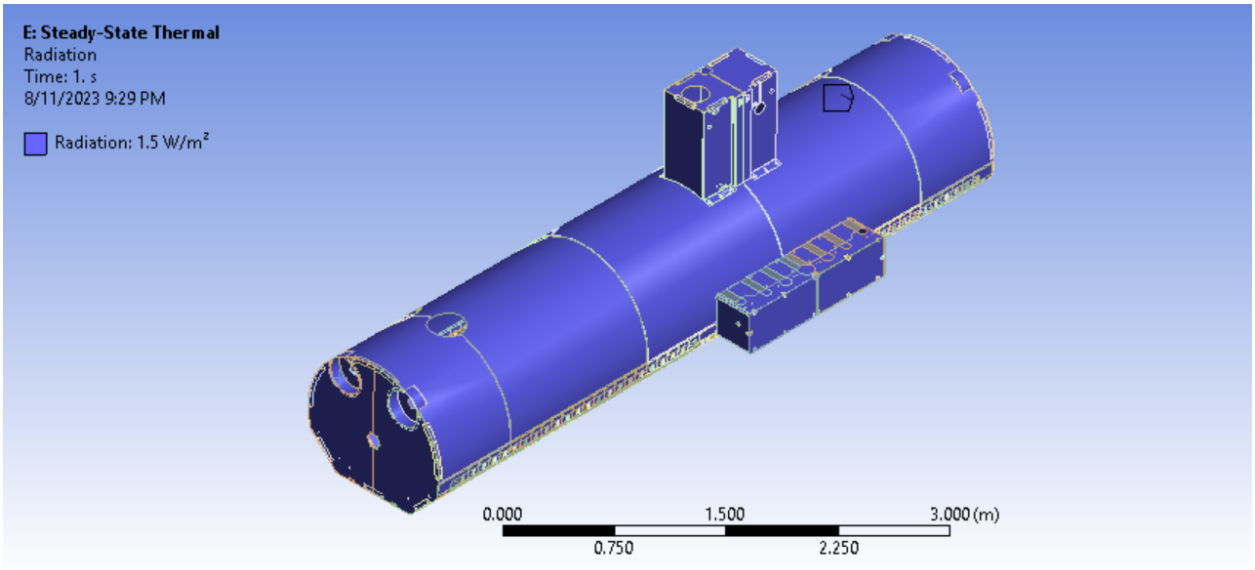

Figure 3.19: Radiation heat load

A third type of heat load in the model is a heat load that is applied to existing geometry in the model. The heat sources in Table 3.1 that fall under this category are the viewports, the cryo port, and the current leads, which can be seen in Figures 3.20 through 3.22. All three of these heat loads are applied to circular edges in the model near the heat source. The heat load is applied to existing geometry since these three heat sources do not have thermal straps connecting them to the thermal shield. These heat sources are also typically closer to the thermal shield than the other heat sources already discussed. The heat load for the view port heat source is applied to the circle edges on the attachment on the end caps. On that attachment, there is a quartz window that gives visual into the thermal shield. In order to allow visual, there cannot be insulation covering the view port. Since there is less insulation at the view ports, more heat is allowed through. The heat load at view ports accounts for this extra heat. The cryoport heat load is applied to an edge on the top of the side port. The cryoport heat load represents the heat applied to the thermal shield from the helium supply pipes. The final and most important heat source is the current lead heat source. The current leads have a static and dynamic heat load, which are applied to five groups of holes on the lower thermal shield. Since the current leads are very crucial to the thermal simulation, the next section will analyze the current leads further.

(a) (b)

Figure 3.20: View port heat load (a) view port in SSR1 CAD model (F10142933); (b) view port heat load

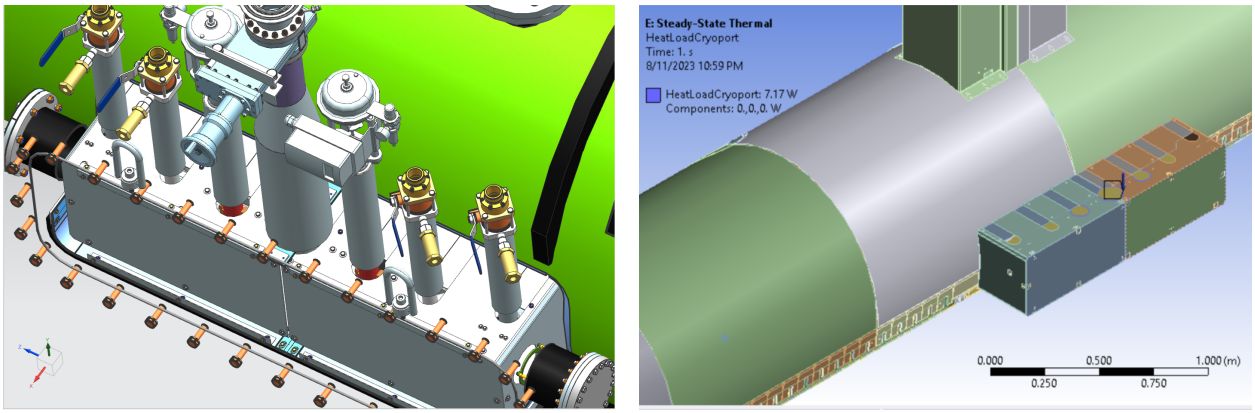

(a) (b) Cryoport heat load

Figure 3.21: Cyoport heat load (a) cryoport in SSR1 CAD model (F10142933); (b) cryoport heat load

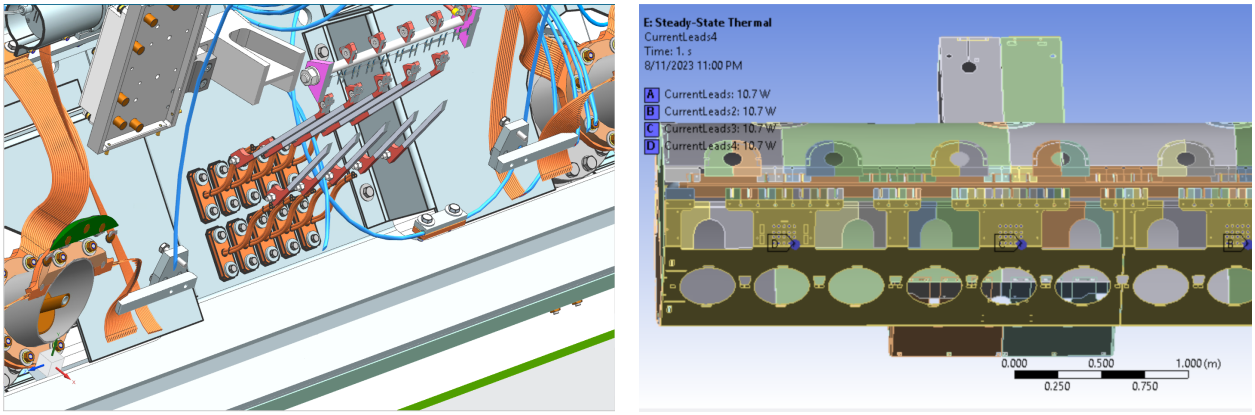

(a) (b)

Figure 3.22: Current lead heat load (a) current leads in SSR1 CAD model (F10142933); (b) current lead heat load

3.4 Current Leads

Unfortunately, the current leads introduce a problem that may lead to a highten chance of the thermal shield exceeding the 68 Kelvin limit. Exceeding the temperature limit is especially bad for the current leads. The current leads are superconducting and are used to provide electricity to the superconducting magnets inside of the thermal shield [33]. These

magnets must remain under 4.2 Kelvin to keep their superconducting properties. As a result, superconducting leads are used to provide electricity to prevent excess heat from reaching the magnet. The temperature limit of the thermal shield is set at 68 Kelvin specifically to ensure the current leads remain superconducting.

The current leads have both a static and dynamic heat load [31], [33]. When the beamline is active, a total of around 21 Watts of energy is deposited onto the thermal shield at each of the 4 current lead locations. Out of all the heat loads, the current leads have the most impact. The amount and locations of the current leads magnify the problem. The lower shield is connected to the extrusion, meaning the heat from the current leads has an easy path to the coldest section of the thermal shield. The lower shield also has larger welds than the upper shield, allowing for more heat to be transferred. Unfortunately, the positives of the location cannot outweigh the negatives of the current leads. The lower shield is an advantageous location for the current leads, however, there is also a high density of heat loads at that location. The side of the thermal shield where the current leads are located has 4 current lead heat loads, heat from the radiation, 8 coupler heat loads on the extrusion, and the instrumentation heat loads on the extrusion. By the time the helium in the extrusion reaches the area of the current lead furthest from the helium source, the helium has already passed most of the heat loads on the thermal shield and has been heated up substantially. The problems discussed above give a clearer picture of the issues the current leads present. The accumulation of all these problems leads to the thermal shield areas surrounding the current leads to heat up at a faster rate than the rest of the thermal shield. The higher temperature from this development not only affects the areas near the current leads but also has a negative impact on the sections of the thermal shield further down the extrusion.

To summarize, this section focused on the setup of the thermal shield steady-state thermal simulation. The decision to use a FEM program for analysis was decided back in Chapter 2, Chapter 3 focused on the setup of that FEM simulation. The different sections of the thermal

shield, the connections between the sections, the different heat loads on the thermal shield, and the importance of the current leads were discussed. The following section (Chapter 4) will examine the results from the simulation that has been set up and further discuss any concerns that arise from those results.

CHAPTER 4

RESULTS

4.1 Baseline Results

The baseline helium properties were provided by Fermilab engineer Jacopo Bernardini and were derived from previous cryomodule testing. These specific property values and results have been dubbed the "baseline" results since the helium parameters used are the current planned values for the helium. The baseline results use a helium inlet temperature of 46 Kelvin and a mass flow rate of 3.5 grams per second. Figure 4.1 shows the baseline results for the Steady-State thermal simulation. Any future modifications must be compared

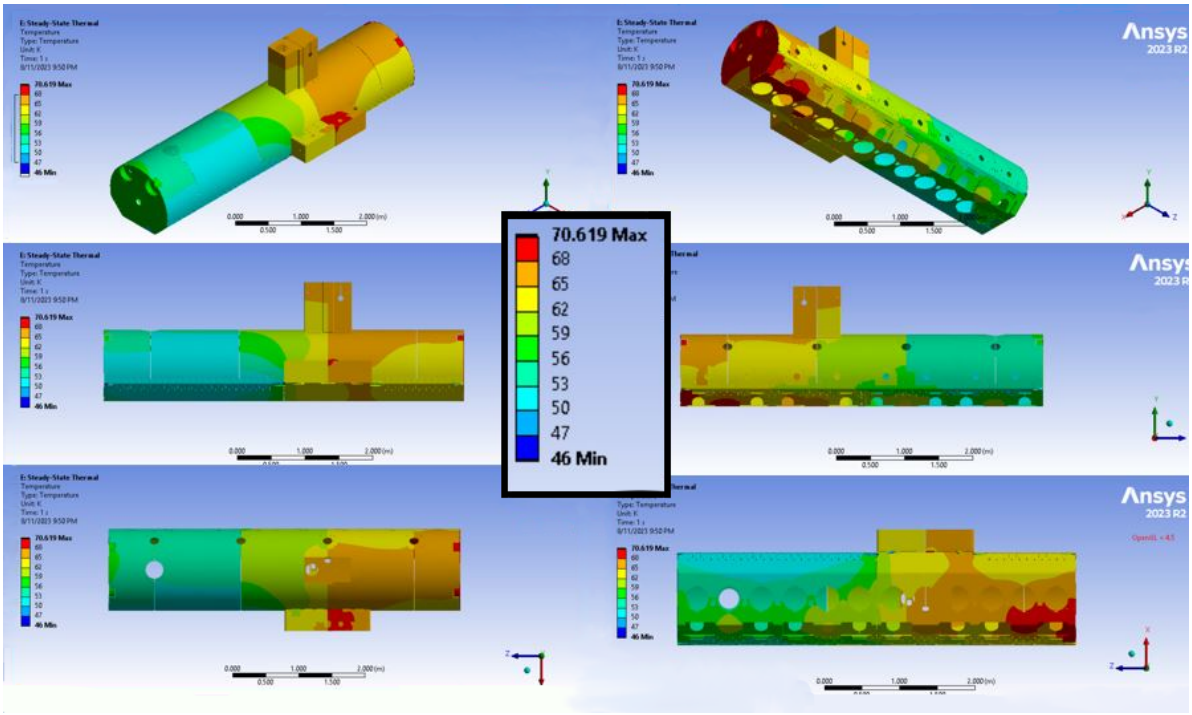

Figure 4.1: Baseline results of steady-state thermal simulation

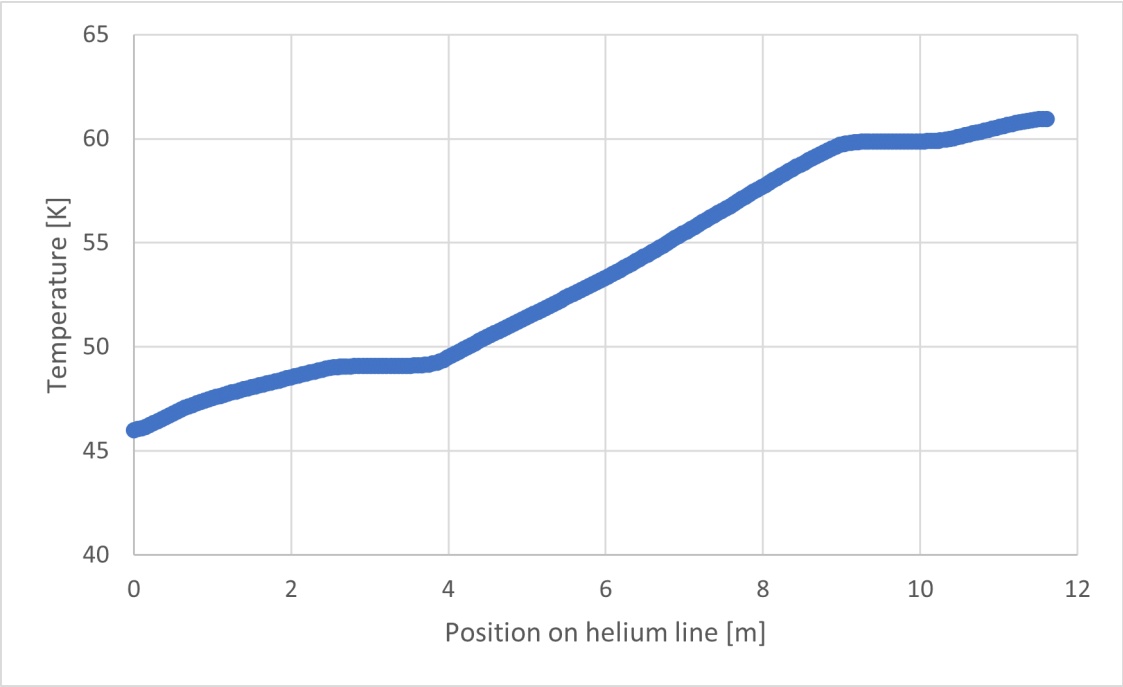

Figure 4.2: The increasing temperature of the helium within the extrusion where the horizontal sections correspond with transfer elbows

against these baseline results.

All of the areas colored red in the results are areas that exceed the allowable temperature of the thermal shield, 68 Kelvin. As expected, the temperature of the thermal shield gradually increases along the span of the thermal shield. At least that is the case, until the second elbow of the extrusion. Looking more closely at the thermal results and Figure 4.3, it can be seen that the temperature on the second elbow is less than the temperature on the preceding long section. Figure 4.2 graphs the temperature of the helium against its location in the extrusion. Meanwhile, Figure 4.3 shows the temperatures on the different sections of the extrusion, and also more clearly labels the different sections of the extrusion.

From the graph, it can be seen that the temperature of the helium is always increasing. The location of the elbow regions on the extrusion can even be clearly seen on the graph, these regions have a less pronounced slope since they are not in direct contact with the

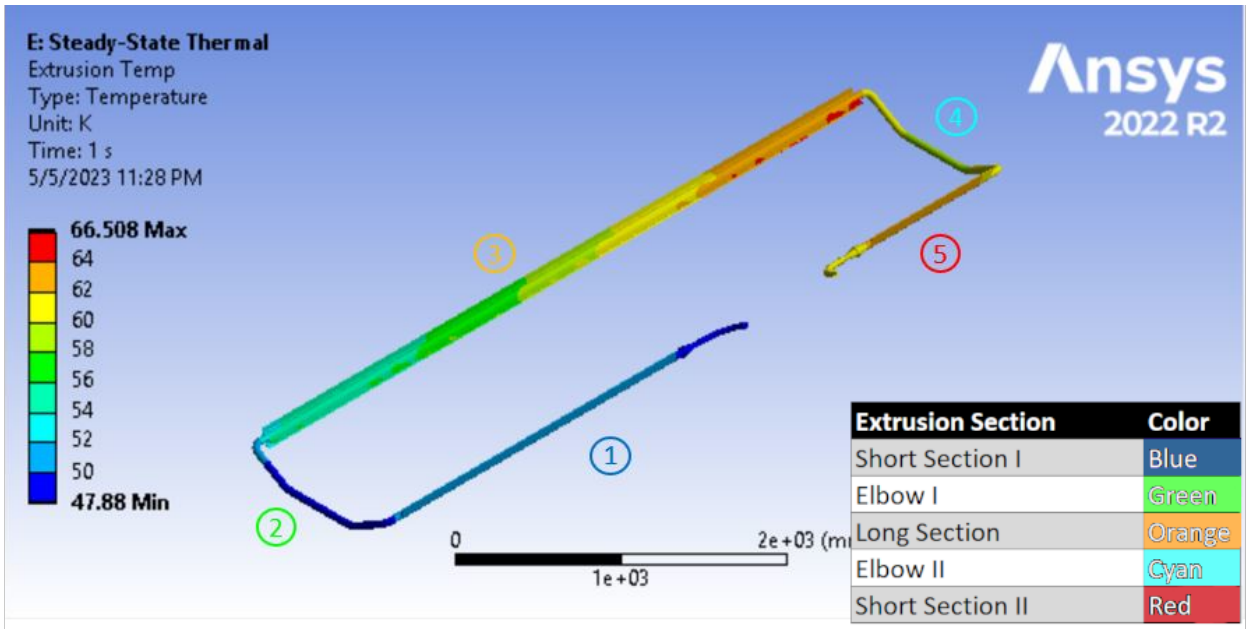

Figure 4.3: Results from Ansys showing the different temperatures on the extrusion and the name of the different sections

thermal shield. The almost horizontal slope regions of the extrusion elbows also have the added benefit of reinvigorating the heat absorption of the following sections of the extrusion. Figure 4.2 proves that the temperature of the helium is always increasing, which means the temperature of the helium is not the cause of the temperature drop between the long section (section 3 on Figure 4.3) of the extrusion and the second elbow (section 4 on Figure 4.3) of the extrusion. Instead, the material limitations of the extrusion are the most likely culprit. The most likely explanation is that the limit of how much heat the material of the extrusion could transfer into the helium was reached. The abundance of heat loads near the long straight section of the extrusion only reinforces this explanation. Reaching the limits of a material property would also explain why the straight section of the extrusion is much hotter, while the proceeding second elbow section is colder due to the lack of heat loads and not making direct contact with the thermal shield.

4.2 Helium Properties

The simplest solution to the high-temperature problem of the thermal shield is modifying the helium properties. Both increasing the mass flow rate and decreasing the inlet temperature of the helium, used to cool the thermal shield, would lower the temperature drastically. Changing the helium properties requires no design modifications and no additions to the thermal shield or cryomodule. The only changes that may be required would be to the cryoplant and the appropriate cryogenic distribution system (CDS) units. However, changing either of the helium properties also has the consequence of increasing the lifelong cost of the project.

Figure 4.4 shows the results of a thermal shield simulation using a helium mass flow rate of 5.5 [g/s]. The baseline results from Figure 4.1 used a mass flow rate of 3.5 [g/s],

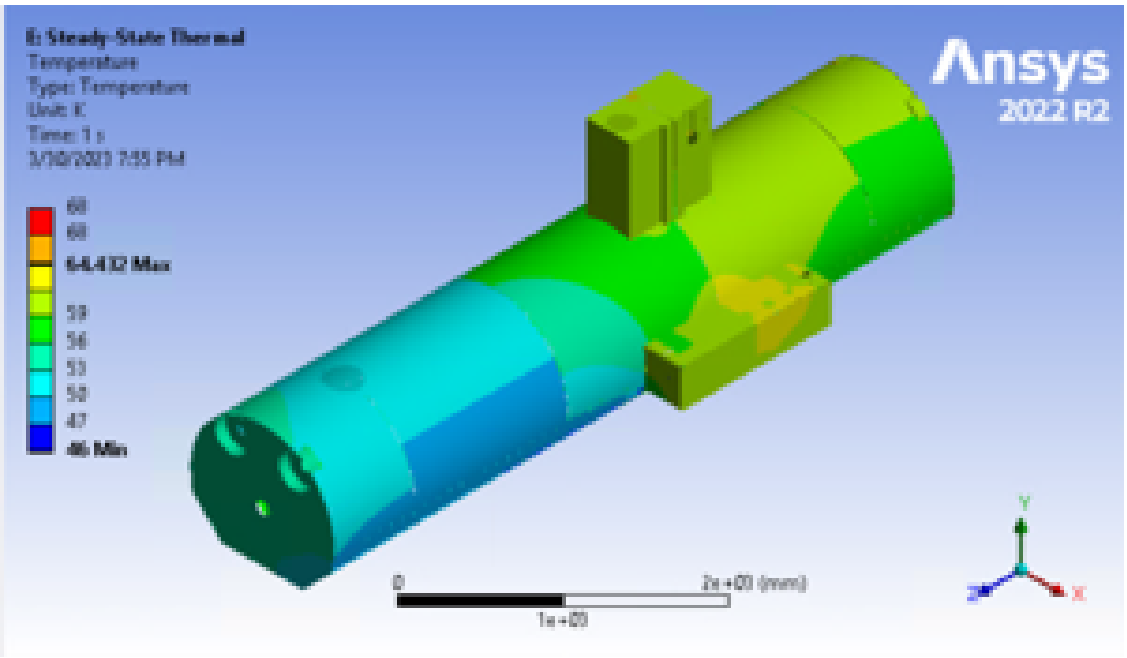

Figure 4.4: Thermal shield temperature results with a mass flow rate of 5.5 [g/s]
[t!]

almost half that of the results from Figure 4.4. Increasing the mass flow rate drastically lowered the temperature of the entire thermal shield. The overall decrease in temperature is expected based on Equation 2.8 where increasing the mass flow rate also increases the convection coefficient, resulting in better heat transfer. Increasing the mass flow rate also increases the total amount of helium in the extrusion, resulting in an increased capacity for absorbing heat. Unfortunately, increasing the mass flow rate also increases the amount of helium that has to be cooled over the life of the project. The increase in helium amount also increases the amount of required energy and strain of the cryoplant. The costs of these additions remain throughout the life of the cryomodule.

Figure 4.5 gives a more detailed look into the effects that different mass flow rates have on the temperature of the thermal shield. The different parameters examined in Figure 4.5 represent the highest temperature on the thermal shield (which is also the temperature at the final current lead location), the average temperature of the thermal shield, the highest

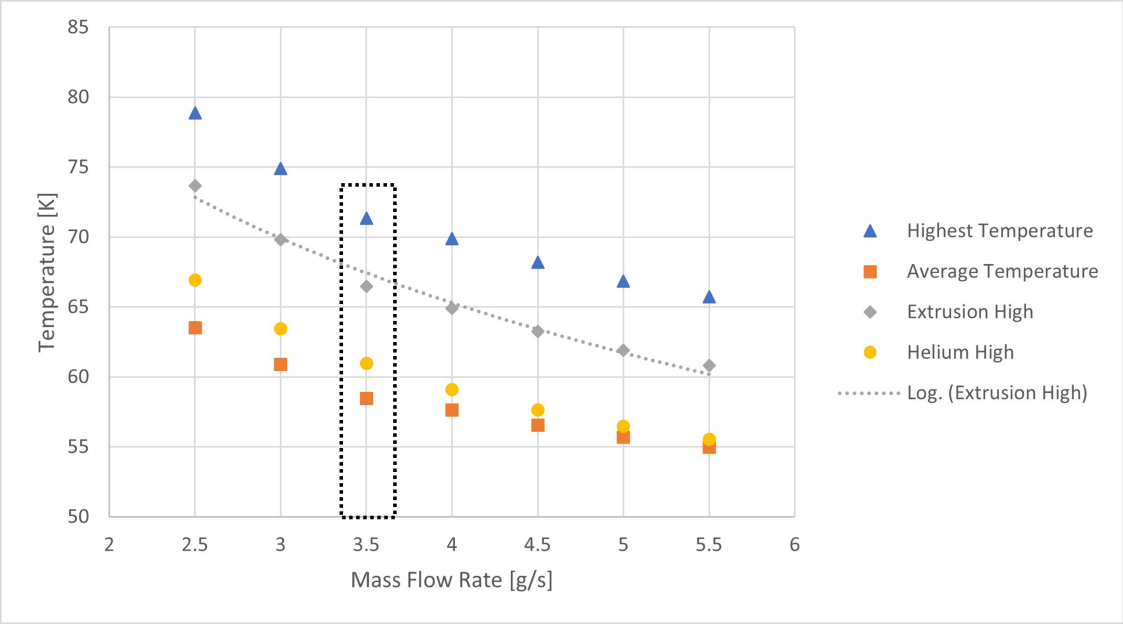

Figure 4.5: Graph visualizing the trend on the temperature of changing the mass flow rate (baseline conditions boxed with dashed lines); logarithmic trendline has a R^2 value of 98.16%

temperature on the extrusion, and the highest temperature on the helium line. The combination of these four parameters displays how each part of the thermal shield model is affected by a modification. The different data points are gathered from simulations where only the mass flow rate is changed. An obvious downward trend in overall temperature can be seen as the mass flow rate increases. Based on the data gathered for Figure 4.5 lowering the temperature of the thermal shield to around 68 Kelvin would require a mass flow rate of around 4.5 [g/s]. The logarithmic trend seen when comparing the different values on Figure 4.5 means the effects of increasing the mass flow rate diminish the more that the mass flow rate is increased.

Figure 4.6 shows the results of a thermal shield simulation where the inlet temperature of the helium is 34 Kelvin. Lowering the temperature of the helium by 12 Kelvin drastically cooled the entirety of the thermal shield. The decrease in the temperature of the helium resulted in the difference of temperatures between the extrusion and thermal shield increasing. The increase in the temperature gradient also improves the heat transfer, allowing for more heat to be removed from the thermal shield. The largest consequence of lowering the helium inlet temperature is that the amount of resources used also increases. Using colder

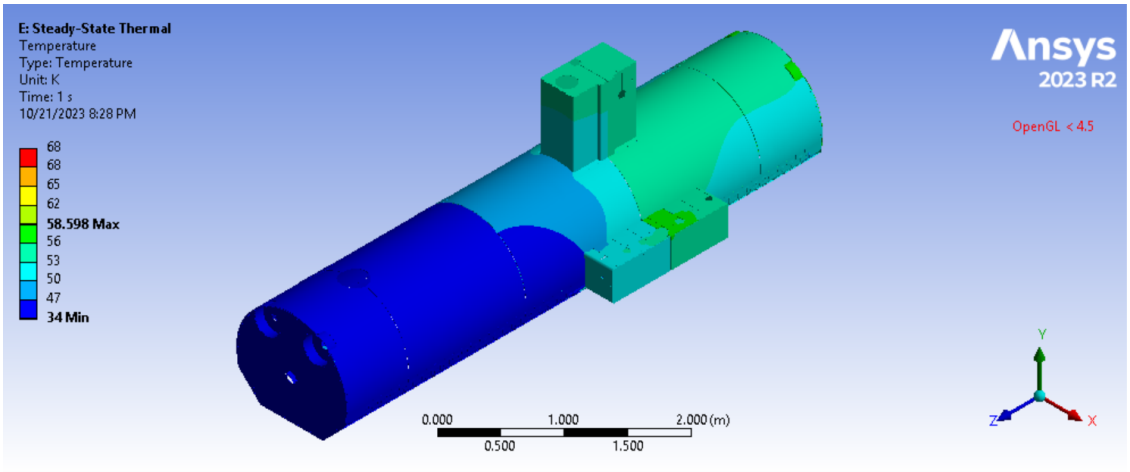

Figure 4.6: Thermal shield temperature results using a helium inlet temperature of 34 Kelvin

helium will add additional strain to the cryoplant and will increase the amount of energy used by the cryoplant. Both of these conditions increase the cost throughout the entire life of the project.

Figure 4.7 graphs the trends of different parameters as the inlet temperature of the helium varies. The same four parameters that were used in Figure 4.5 were used for Figure 4.7. From these four parameters, it can be seen that lowering the helium inlet temperature also lowers the overall temperature of the thermal shield. An inlet temperature of around 43 Kelvin would be required to lower the max temperature on the thermal shield to 68 Kelvin. The linear trend of the values seen in Figure 4.7 shows that, for the range measured, changing the inlet temperature is more consistent than changing the mass flow rate. However, cooling helium to increasing colder temperatures would incur nonlinear costs from the cryoplant.

Unfortunately, the optimal modification in helium parameters is not known. The amount of wattage required to further lower the helium inlet temperature and lower the temperature

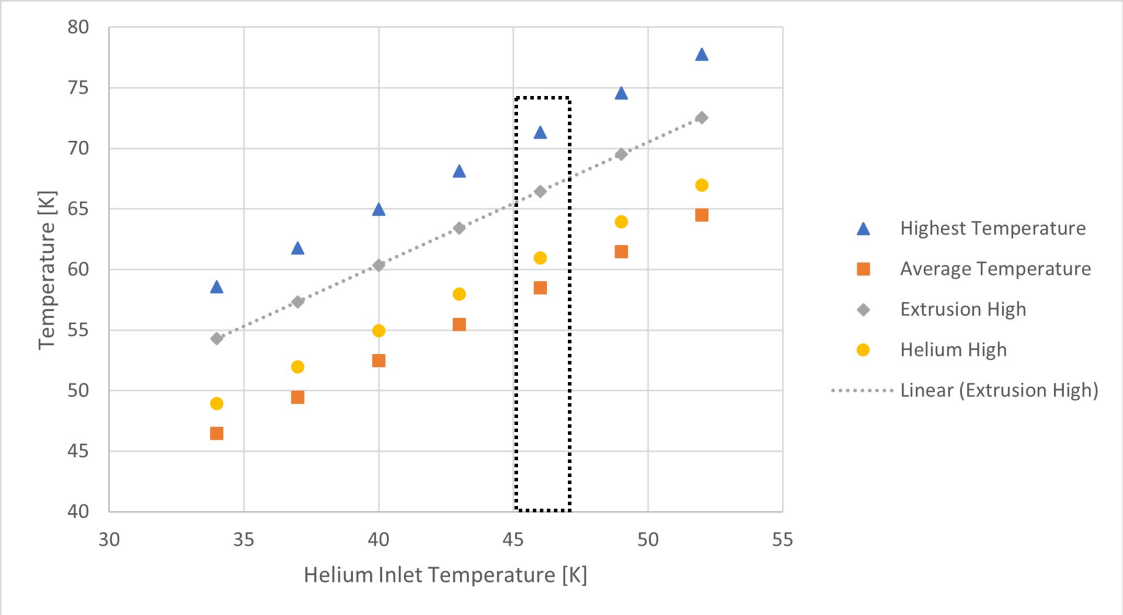

Figure 4.7: Graph visualizing the effects modifying the inlet temperature has on the thermal shield (baseline conditions boxed in dashed lines); linear trendline has a R^2 value of 100%

of excess helium remains mostly consistent. However, the efficiency of each change is not known. Further analysis of the two helium parameters and the cryoplant would be required. Depending on the findings, the optimal strategy may even involve a change to both helium parameters. Regardless, focusing on the heat transfer of crucial thermal shield locations may help in alleviating the mass flow rate and inlet temperature required.

4.2.1 Copper Plate Addition

Figure 4.8 provides a clearer view of the high-temperature area on the baseline results. The temperature first exceeds 68 Kelvin in the area of the final set of current leads, the current leads furthest from the inlet location of the helium. The high heat from this location spreads throughout the sections of the thermal shield furthest any cooling. The bottom of the lower shield, seen in Figure 4.9, is blocked from any cooling by the high heat of the final current leads. Meanwhile, neither of the end caps is directly connected to the extrusion. The lack of direct contact allows for the high temperatures of the adjacent lower shield to increase the temperature of the end caps furthest from the inlet location of the helium. The

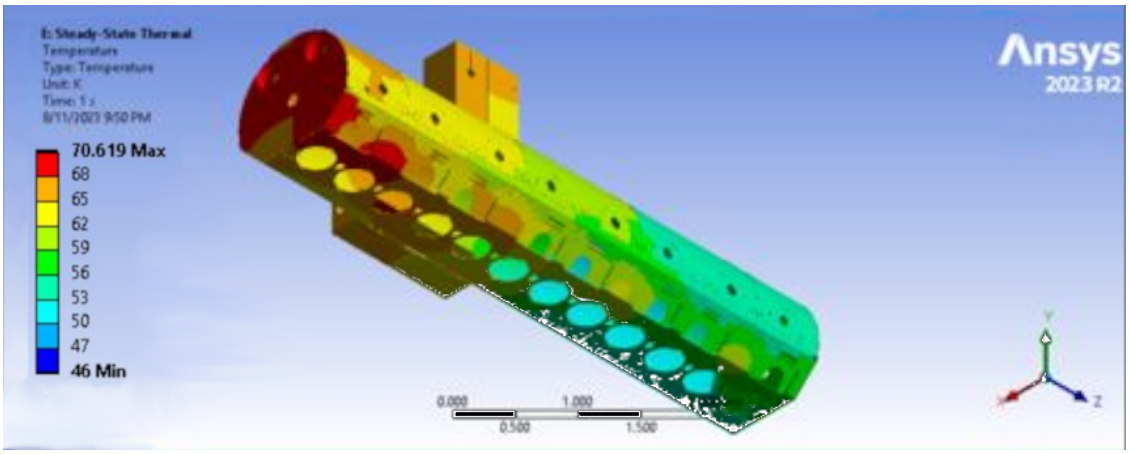

Figure 4.8: Baseline results back view, better view of high-temperature areas

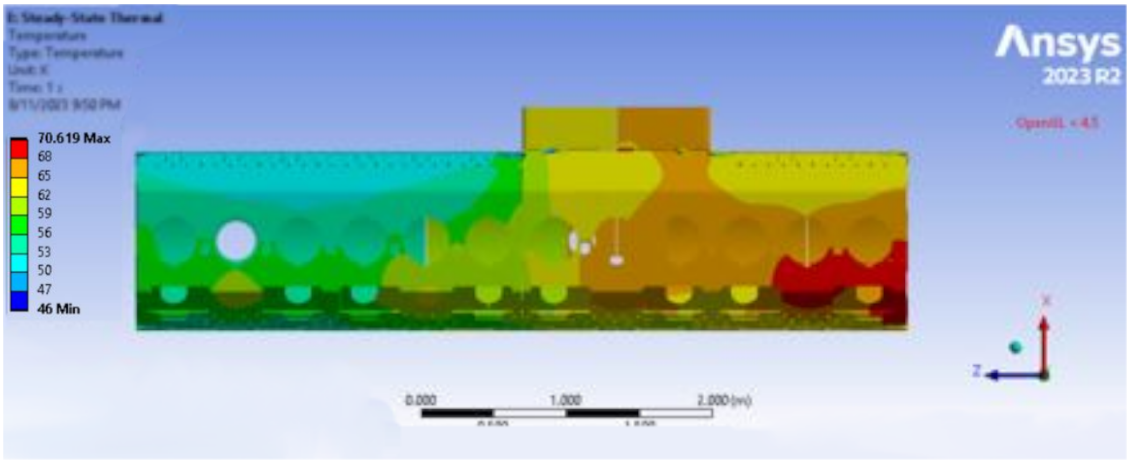

Figure 4.9: High temperatures on the underside of the lower shield

high temperatures on the end caps caused by the lack of contact can be seen in Figure 4.10. Since the main culprit of the high temperatures is the high heat area of the final current leads, lowering the temperature of only the region around the final set of current leads could resolve the issue. If the area around the final set of current leads was at a lower temperature, that may prevent the adjacent areas from exceeding the 68 Kelvin temperature limit.

The design proposed in this paper is a copper plate inside of the thermal shield, above the cutouts for the current leads. A CAD representation of the copper plate and its proposed location can be seen in Figure 4.11. If the copper plate idea were to be adopted, the heat load from the current leads would be applied only to the copper plate. Thermally insulated spacers would also prevent any of the heat of the final set of current leads from reaching the thermal shield. The copper plate would still have to be kept below the 68 Kelvin temperature limit to ensure the current leads remain functional. The proposed design also plans to use thermal straps connected to colder sections of the thermal shield as cooling. The thermal straps would help disperse the heat to other less crucial locations on the thermal shield.

Multiple parameters and properties can be modified and analyzed when designing an attachment like the copper plate. For example, the dimensions of the plate must fit, and not interfere with, the current design of the thermal shield. However, changing the dimensions

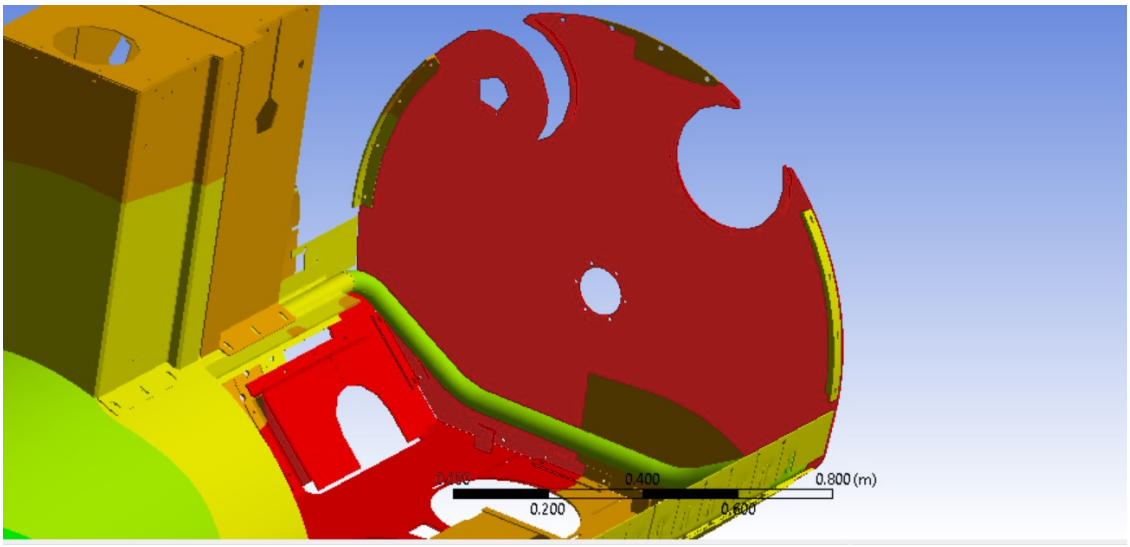

Figure 4.10: Temperature difference between the extrusion and the end caps

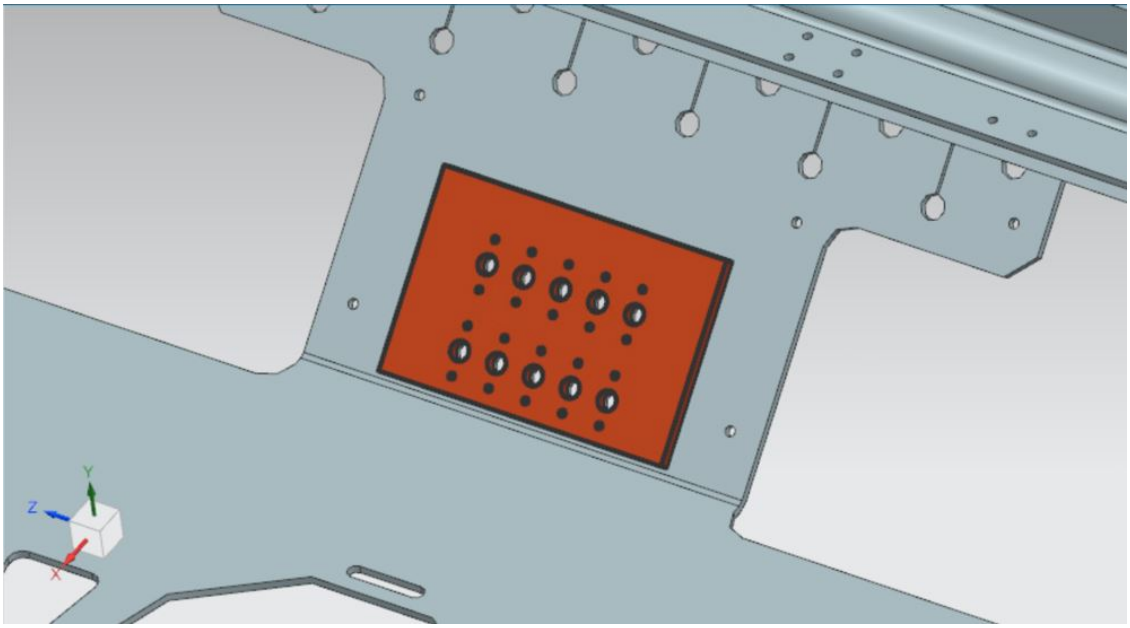

Figure 4.11: Proposed copper plate idea and location within thermal shield NX model (F10191721)

also affects the heat transfer, a detailed analysis could be conducted on the most advantageous geometry. Copper was picked as the material for the plate due to its well-known high thermal conductivity. However, there might be a different material that performs more

efficiently. The performance of the material would have to be contrasted against its manufacturability and obtainability. A different comprehensive analysis could also be done on the installation of the plate, finding the best method, time, and location of the installation. Unfortunately, time is limited, and not every aspect of the proposed copper plate addition could be analyzed in depth. The thermal straps are a crucial component of the attachment, therefore, the thermal straps received a more comprehensive analysis.

A simple steady-state thermal simulation was created to better analyze the thermal strap on the copper plate. Figure 4.12 shows the geometry of the copper plate simulation. A separate model was created in order to not clutter the original thermal shield model. Adding the copper plate to the thermal shield model would increase the solution time and take longer to create. The solitary copper plate model is sufficient for this analysis since only the different thermal strap connection locations are being analyzed.

The model is a rectangle with dimensions that fit in the location available inside of the thermal shield. A rectangle was chosen since it provided the most area for thermal straps. Meanwhile, a thickness of 10 [mm] was used after a 1D heat analysis of the plate predicted increasing the thickness further would have diminishing results.

(a) (b)

Figure 4.12: Copper plate simulation (a) isometric view of the copper plate model; (b) side view of the copper plate model

The different openings for the current leads and possible connection points were also carefully placed in their approximate location. The same type of OFHC copper that is used for the thermal straps was also chosen as the material for the plate. OFHC copper was chosen since it is highly conductive and easily obtainable by Fermilab. Tests on the effects 3 different alloys of OFHC copper (RRR=50,100,300) have on the overall temperature were conducted. The results found that the RRR value of the copper does not seem to have a significant effect.

Different orientations of the thermal strap were also tested. The thermal strap positions seen in Figure 4.12 performed the best since they provide the best heat paths between the straps and the current lead heat loads. The thermal strap representations used for the copper plate analysis are the same that were discussed in the Methodology section. Further analysis of the positioning and number of thermal straps is recommended. A subsequent more detailed, future analysis may find a more optimal number and position of the thermal straps.

The copper plate model was first tested assuming connections between the copper plate and the nearest regions of the thermal shield. Figure 4.13 displays the results from the first test. Unfortunately, the temperature on the copper plate does exceed the 68 Kelvin temperature limit. Connecting to a colder region of the thermal shield will be required. The top four thermal straps used temperature values from the region of the extrusion directly above the plate. Meanwhile, the four side thermal straps used temperature values from the lower thermal shield. The temperature values for the thermal straps were gathered from the thermal shield baseline results. Figures 4.14 and 4.15 show temperature probes that were used on the thermal shield simulation to gather the temperature values.

Deciding on possible thermal strap locations is a complex endeavor. The farther the location is the copper plate, the more complicated the thermal strap becomes. The coldest regions of the thermal shield are also some of the furthest away. Connecting the copper

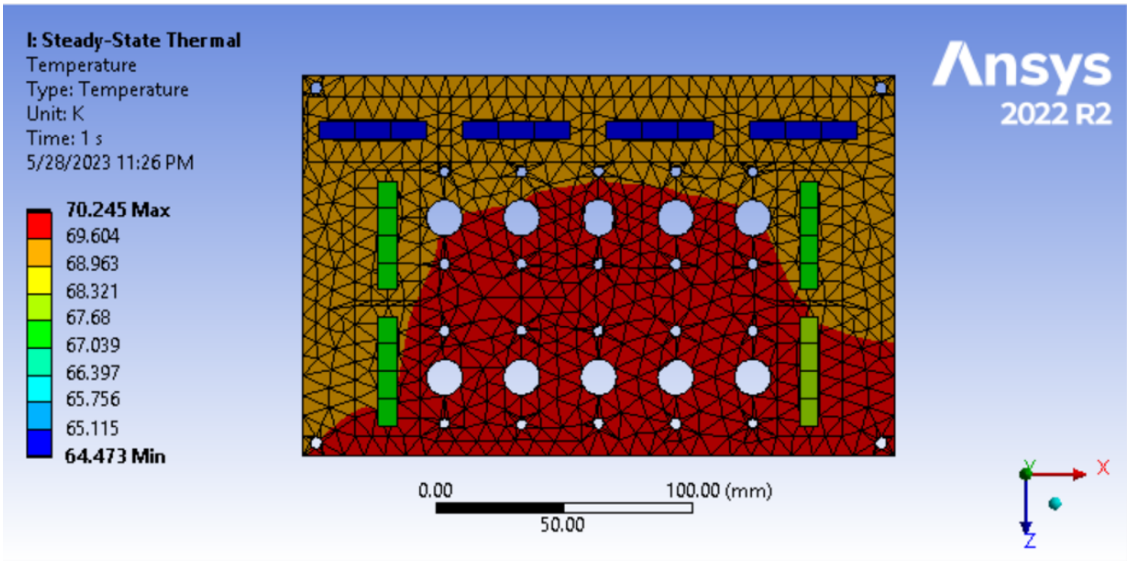

Figure 4.13: Results of the first copper plate test assuming nearby connection points

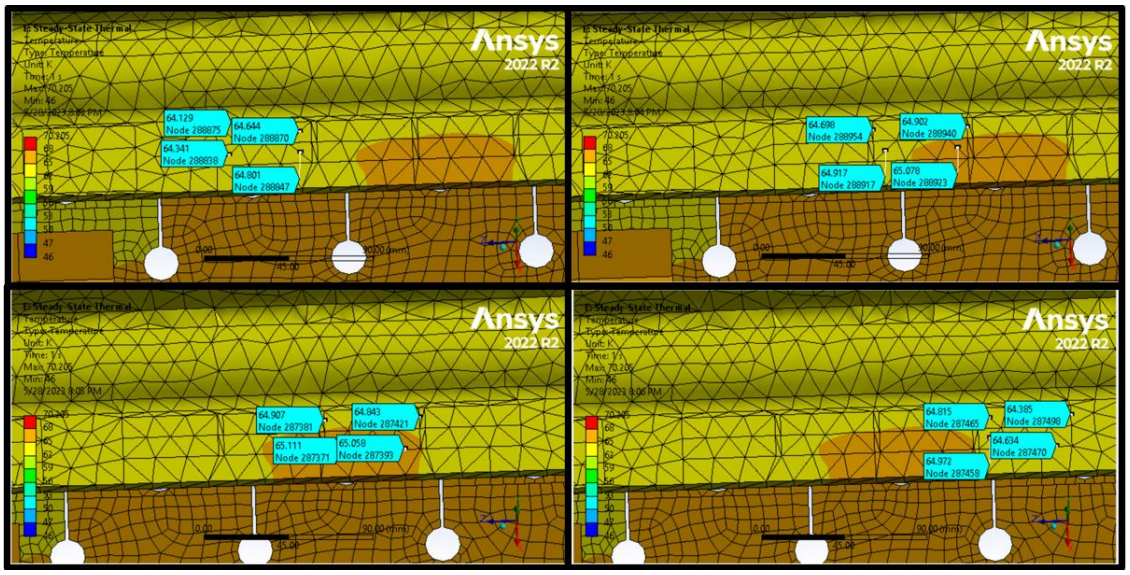

Figure 4.14: Thermal shield extrusion temperature probes

plate to the coldest regions of the thermal shield would result in very long thermal straps that will need to maneuver through the internals of the cryomodule. The complexity of this problem makes a detailed analysis time-consuming and does not guarantee a preferable result. Before analyzing realistic thermal strap connection locations, the extent of the effects colder thermal straps have should be analyzed.

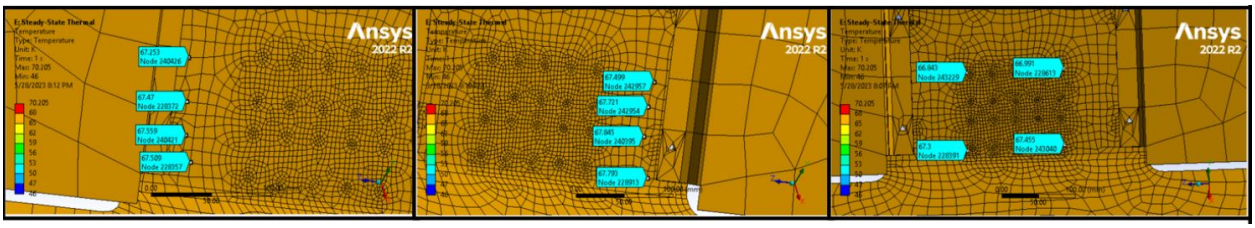

Figure 4.15: Lower thermal shield temperature probes

Figure 4.16 compares the thermal results of the copper plate when connected to regions with different temperatures. The results seen in Figure 4.16 show that connecting the copper plate to colder sections of the thermal shield does have a significant effect on the temperature of the plate. The temperatures of the thermal straps used for the tests in Figure 4.16 mimic the temperature spread of the thermal shield. The "tested" temperature was set as the maximum thermal strap temperature. The rest of the thermal strap temperatures were then decreased by similar amounts to temperature spreads gathered using the method seen in Figures 4.14 and 4.15.

Connecting the copper plate to colder regions of the thermal shield has proven to decrease the temperature of the plate. However, there is no guarantee that colder regions will continuously decrease the temperature. In order to ensure that there is no temperature where the effect diminishes, a variety of different thermal strap temperatures were tested and plotted.

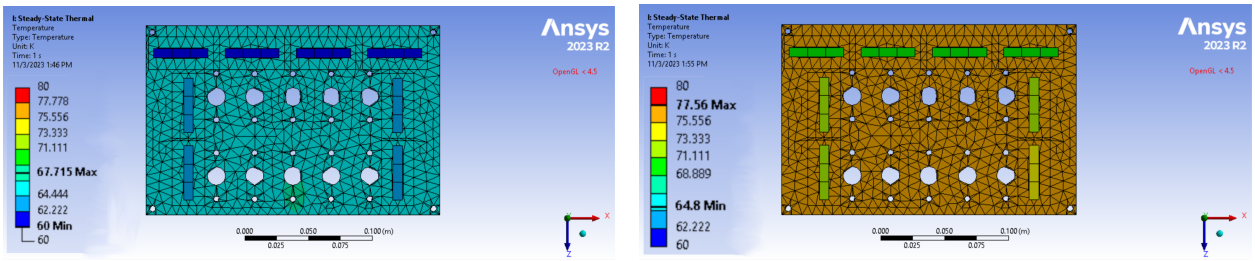

(a) (b)

Figure 4.16: Comparison of different copper plate connection temperature results (a) plate connected to regions of the thermal shield around 60 Kelvin; (b) plate connected to regions of the thermal shield around 70 Kelvin

The results of these thermal strap tests can be seen in Figure 4.17. Based on Figure 4.17 the effect colder locations have on the copper plate is consistent. With this information, it can be deduced that it will always be more beneficial to attach the thermal straps to colder regions since there is no lowest temperature where the thermal straps' effectiveness dwindles. Figure 4.17 even shows that reaching a temperature of 68 Kelvin would only require a thermal shield region around 62 Kelvin.

The 62 Kelvin prediction is an estimate from a simple model, however, it does provide a starting point and does predict an achievable temperature on the thermal shield. Further analysis of the effects of an addition like the copper plate will be required to justify its creation. An analysis adding the copper plate to the thermal shield simulation is recommended. The simple model tested only shows how the copper plate and, by association, the set of current leads furthest from the helium inlet location will be affected. However, the effect that the copper plate idea has on the overall thermal shield still needs to be analyzed. Once

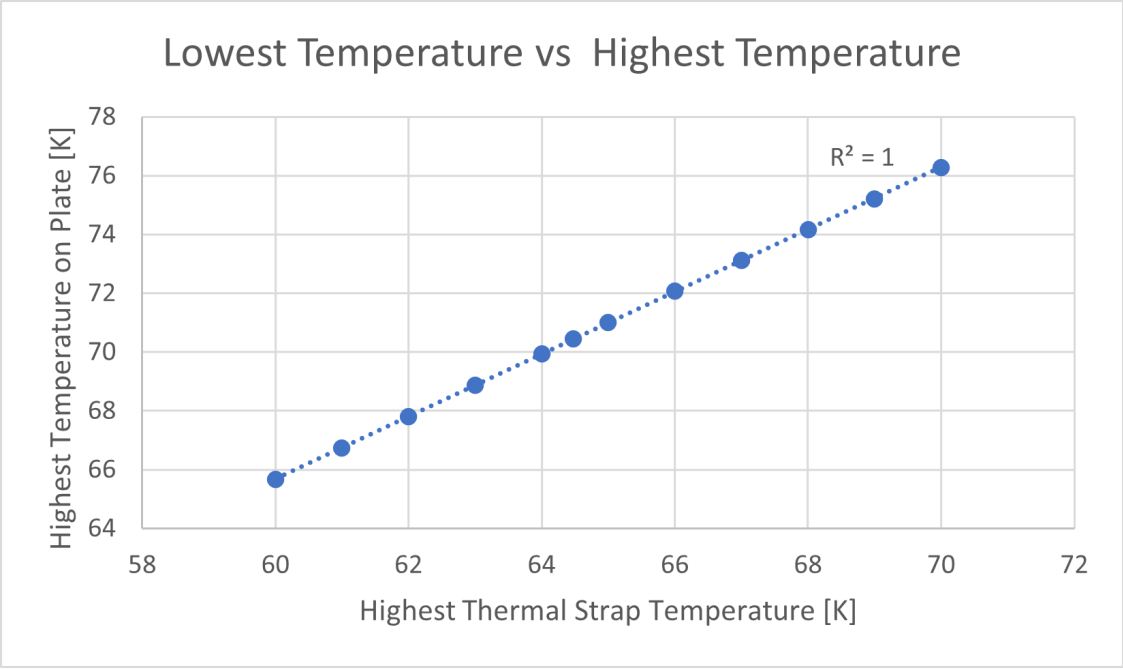

Figure 4.17: Plot showing the different thermal strap temperature tests

an ideal connection location on the thermal shield is chosen for the thermal straps on the copper plate, an analysis is needed to observe the ramifications of moving that current lead heat load.

The changes in temperature distribution caused by the copper plate thermal strap may also have other negative consequences. The future analysis recommended should ensure that no other sections of the thermal shield exceed to 68 Kelvin limit. The temperature values used on the copper plate thermal shield for the areas in contact with the thermal shield will also vary depending on where the copper plate thermal straps are connected. G10 was used as the material for the spacers due to its use as a thermal insulator, however, the recommended future analysis should also inspect the connection points between the copper plate and the thermal shield.

CHAPTER 5

CONCLUSION

5.1 Research Question

In conclusion, the created thermal simulation of the SSR1 thermal shield predicts that the allowable temperature of the thermal shield will be exceeded. According to the simulation, certain areas near the end of the thermal shield's helium path will exceed the allowable temperature limit of 68 Kelvin. The main causes of these high temperatures are the accumulation of high heat loads throughout the thermal shield, their concentration at crucial sections of the thermal shield, and the helium properties used. The values used for the helium properties are the planned values. Since these helium properties are currently only planned, they are one of the few properties that can be modified.

5.2 Summary and Reflection

An Ansys FEM Steady-State Thermal simulation was used to estimate the temperatures on the SSR1 thermal shield. The simulation was specifically set up to estimate the temperatures of the thermal shield during beamline operation when the thermal shield would be at its maximum temperature. Based on the results gathered, the simulation seems to do an adequate job of estimating the temperatures of the thermal shield, even with all the required heat loads and special conditions. The simulation results make physical sense and when changes are made to the boundary conditions the results change as expected.

All of the simulation files and data produced are in the possession of Fermilab. Integrating any future additions/modifications to the model should be a straightforward endeavor. During the fabrication of the simulation, an emphasis was made to clearly label the different sections of the simulation. The different contacts used in the simulation were organized into labeled folders depending on the thermal shield part with which the contact interacts. The notes and PowerPoints generated during the research are also accessible to Fermilab. The notes and PowerPoints contain information detailing the setup of the simulation. For example, the notes contain information on all the different contacts used in the simulation, the setup and justification behind the boundary conditions, geometry edits that were made in the simulation, and a plethora of other information. Hopefully, all of this information will be beneficial to any future modifications of the simulation, or to any future personnel working on a similar simulation.

The thermal shield simulation was also set up to make testing different helium inlet properties convenient. The boundary conditions for the mass flow rate and inlet temperature of the helium are clearly labeled. All geometry selections for the mass flow rate and inlet temperature boundary conditions have already been made. Testing a different helium inlet temperature only requires the new inlet temperature to be entered into the magnitude section of the boundary condition. Meanwhile, testing a different mass flow rate requires the new mass flow rate magnitude and the helium convection coefficients to be updated. The supplied notes detail the process of calculating and updating the convection coefficients.

The simulation for the copper plate addition also provides realistic results. However, the copper plate simulation is more simple and separate from the thermal shield simulation. The copper plate simulation was made separate from the thermal shield simulation in order to not slow down and over-complicate the already complex thermal shield simulation. The current simple copper plate simulation gives a preliminary look into how such an addition may benefit the thermal shield.

5.3 Future Recommendations

Based on the findings in this paper, there are two main remedies to the SSR1 thermal shield temperature problems. The first solution would be changing the properties of the helium used such that it will lower the overall temperature of the thermal shield. The second solution would be editing the design of the thermal shield in a way that prevents any location from exceeding the 68 Kelvin temperature limit.

Changing the properties of the helium used by the thermal shield will involve either increasing the mass flow rate, decreasing the inlet temperature, or a combination of both. The largest advantage of changing the helium properties is the simplicity of the solution. The helium property solution would not require any new designs or parts. Instead, it would be a simple modification to cryoplant and the appropriate cryogenic distribution system (CDS) unit. However, the cost of this solution would continuously increase over time. Since either more helium needs to be cooled, or the helium needs to be cooled to a colder temperature, the amount of electricity needed increases. This increase would remain throughout the entire life of the SSR1 cryomodule.

Editing the design of the thermal shield is another route that could be taken, and could even result in a more affordable solution in the "long term." The results from the copper plate simulation predict the addition could be beneficial to the thermal shield. However, its implementation depends on the cost and the feasibility of the thermal strap connections. If the price of the design is less than the estimated additional costs of changing the helium properties and practicable thermal strap placements are found this solution is the obvious choice. Different designs and thermal strap placements can be tested to achieve the best results.

The final recommendation for the future would be to integrate the copper plate into the thermal shield simulation. Due to a lack of time, the copper plate design was not able to be implemented into the SSR1 thermal shield simulation for this paper. However, the addition of the copper plate to the model would be beneficial in better testing the feasibility of the idea. It is recommended when adding the copper plate to create a new save file for the simulation. By creating a new save file both a simulation with the copper plate and without the copper plate can be analyzed. A model with both the thermal shield and the copper plate would help in quickly testing any future additions or modifications made. For example, different thermal strap connections and different geometries could be tested. Incorporating the copper plate into the thermal shield model would also provide better estimates of the effects of the copper plate. The thermal shield temperatures and thermal strap temperatures used in the simple copper plate simulation were estimates from the approximate locations on the thermal shield model. Adding the copper plate design to the simulation would result in better estimates for those temperatures and help in the optimization of the plate. Further analysis evaluating different geometries of the copper plate, the interfaces of the plate with crucial thermal shield components like the current leads, and different geometric factors of the plate would further optimize the design and installation of the copper plate.

BIBLIOGRAPHY

[1] Fermi National Accelerator Laboratory. "Fermi national accelerator laboratory - history of fermi." Accessed on October 21, 2023. (2023), [Online]. Available: https://history.fnal.gov/history-fermi.html.

[2] Fermi National Accelerator Laboratory. "Key discoveries in particle physics." Accessed on: October 23, 2023. (2023), [Online]. Available: https://www.fnal.gov/pub/science/particle-physics/key-discoveries.html.

[3] Fermi National Accelerator Laboratory. "Muon g-2 experiment at fermilab." Accessed on October 21, 2023. (2023), [Online]. Available: https://muon-g-2.fnal.gov/.

[4] Fermi National Accelerator Laboratory. "Holometer experiment." Accessed on: October 23, 2023. (2023), [Online]. Available: https://holometer.fnal.gov/.

[5] Fermi National Accelerator Laboratory. "Long-baseline neutrino facility and deep underground neutrino experiment (lbnf/dune) at fermilab." Accessed on October 21, 2023. (2023), [Online]. Available: https://lbnf-dune.fnal.gov/.

[6] Fermi National Accelerator Laboratory. "Fermilab particle accelerator complex." Accessed on October 21, 2023. (2023), [Online]. Available: https://www.fnal.gov/pub/science/particle-accelerators/accelerator-complex.html.

[7] Fermi National Accelerator Laboratory. "Fermilab accelerator history." Accessed on October 21, 2023. (2023), [Online]. Available: https://history.fnal.gov/historical/accelerator/accelerator_history.html#:~:text=Originally%2C%20the%20Main%20Ring%20delivered,energies%20of%20over%202%20TeV.

[8] Fermi National Accelerator Laboratory, *PIP-II Project at Fermilab*, Accessed on November 7, 2023, 2023. [Online]. Available: https://pip2.fnal.gov/.

[9] Fermi National Accelerator Laboratory. "Pioneering instrumentation for the particle frontier (pipf) - superconducting radio-frequency technology." Accessed on October 21, 2023. (2023), [Online]. Available: https://pip2.fnal.gov/how-it-works/superconducting-radio-frequency-technology/.

[10] A. Klebaner, C. Boffo, S. K. Chandrasekaran, D. Passarelli, and G. Wu, "Proton improvement plan – ii: Overview of progress in the construction," *JACoW*, vol. SRF2021, May 2022. DOI: 10.18429/JACoW-SRF2021-MOOFAV05. [Online]. Available: https://www.osti.gov/biblio/1898824.

[11] Fermi National Accelerator Laboratory. "Pioneering instrumentation for the particle frontier (pipf) - international partnerships." Accessed on October 21, 2023. (2023), [Online]. Available: https://pip2.fnal.gov/about/international-partnerships/.

[12] Fermi National Accelerator Laboratory. "Lbnf/dune - neutrino beam." Accessed on October 21, 2023. (2023), [Online]. Available: https://lbnf-dune.fnal.gov/how-it-works/neutrino-beam/.

[13] Fermi National Accelerator Laboratory. "Dune fact sheet." Accessed on October 21, 2023. (2023), [Online]. Available: https://news.fnal.gov/wp-content/uploads/dune-fact-sheet.pdf.

[14] Fermi National Accelerator Laboratory. "Pre-excavation work on lbnf/dune begins in south dakota." Accessed on October 21, 2023. (2023), [Online]. Available: https://news.fnal.gov/2019/01/pre-excavation-work-on-lbnf-dune-begins-in-south-dakota/.

[15] Fermi National Accelerator Laboratory. "Pioneering instrumentation for the particle frontier (pipf) - introduction." Accessed on October 21, 2023. (2023), [Online]. Available: https://pip2.fnal.gov/how-it-works/introduction/.

[16] Fermi National Accelerator Laboratory. "Srf cavities lecture." Accessed on October 21, 2023. (2023), [Online]. Available: https://uspas.fnal.gov/materials/21onlineSBU/Cryo/12%20-%20SRF%20Cavities.pdf.

[17] Fermi National Accelerator Laboratory. "Cryomodule design lecture." Accessed on October 21, 2023. (2023), [Online]. Available: https://uspas.fnal.gov/materials/19NewMexico/Cryo/8-CryomoduleDesignLecture.pdf.

[18] Fermi National Accelerator Laboratory. "Superconducting radio-frequency (srf) capabilities at fermilab." Accessed on October 21, 2023. (2023), [Online]. Available: https://td.fnal.gov/srf-capabilities/#Cryo.

[19] D. Passarelli, J. Bernardini, C. Boffo, *et al.*, "Test results of the prototype ssr1 cryomodule for pip-ii at fermilab," Aug. 2021. DOI: 10.18429/JACoW-IPAC2021-THPAB343. [Online]. Available: https://www.osti.gov/biblio/1854783.

[20] Fermi National Accelerator Laboratory. "Pioneering instrumentation for the particle frontier (pipf) - photos and videos." Accessed on October 21, 2023. (2023), [Online]. Available: https://pip2.fnal.gov/about/photos-and-videos/.

[21] A. Barnaba, F. Bucchi, P. Neri, and D. Passarelli, "Experimental modal analysis of ssr1 cryomodule for numerical model tuning and validation," *IOP Conference Series. Materials Science and Engineering*, vol. 1038, no. 1, Feb. 2021. DOI: 10.1088/1757-899x/1038/1/012077.

[22] J. Bernardini, D. Passarelli, V. Roger, *et al.*, *Final design of the pre-production ssr2 cryomodule for pip-ii project at fermilab*, 2022. arXiv: 2209.01282 [physics.acc-ph].

[23] T. Nicol and et al., "Ssr1 cryomodule design for pxie," Sep. 2013. [Online]. Available: https://www.osti.gov/biblio/1128804.

[24] T. Nicol. "Cryomodule design overview." Accessed on October 21, 2023. (2023), [Online]. Available: https://indico.fnal.gov/event/18092/contributions/45667/attachments/28384/35095/Cryomodule_design_overview_-_Cryomodule_design_workshop_-_September_4_2018.pdf.

[25] G. J. Smith, "Thermal / structural analysis of the hb 650 thermal shield," Dec. 2020. DOI: 10.2172/1763408. [Online]. Available: https://www.osti.gov/biblio/1763408.

[26] Y. A. Çengel and A. J. Ghajar, *Fundamentals of Heat and Mass Transfer*, 8th. Wiley, 2017.

[27] P. Bradley and R. Radebaugh, *Properties of Selected Materials at Cryogenic Temperatures*. Boca Raton, FL: CRC Press, 2013, [Online]. [Online]. Available: https://tsapps.nist.gov/publication/get_pdf.cfm?pub_id=913059 (visited on 10/21/2023).

[28] T. N. I. of Standards and Technology, *Nist chemistry webbook*, Accessed: October 22, 2023, 2023. [Online]. Available: https://tsapps.nist.gov/publication/get_pdf.cfm?pub_id=913059.

[29] R. Winterton, "Where did the dittus and boelter equation come from?" *International Journal of Heat and Mass Transfer*, vol. 41, no. 4, pp. 809–810, 1998, ISSN: 0017-9310. DOI: https://doi.org/10.1016/S0017-9310(97)00177-4. [Online]. Available: https://www.sciencedirect.com/science/article/pii/S0017931097001774.

[30] T. Harris. “Be a pinball wizard with contact regions in ansys mechanical.” Accessed: October 23, 2023. (2015), [Online]. Available: https://www.padtinc.com/2015/11/09/be-a-pinball-wizard-with-contact-regions-in-ansys-mechanical/.

[31] S. Chandrasekaran, “Pip-ii cryogenic heat load analysis physics requirement document (pdr),” Fermi National Accelerator Laboratory, Tech. Rep., 2021, ED0008200.

[32] S. Chandrasekaran, “Pip-ii heat load analysis - cryomodules,” Fermilab, Tech. Rep., 2020, ED0008200.

[33] M. Turenne, “Pip-ii ssr cryomodule focusing lens current leads design,” Fermi National Accelerator Laboratory, Tech. Rep., 2022, ED0016800.